The phases and amplitudes of gravity waves propagating and dissipating in the thermosphere: Theory

S. L. Vadas[1] and M. J. Nicolls[2]

Received 1 December 2011; revised 12 March 2012; accepted 20 March 2012; published 23 May 2012.

[1] We derive the high-frequency, compressible, dissipative dispersion and polarization relations for linear acoustic-gravity waves (GWs) and acoustic waves (AWs) in a single-species thermosphere. The wave amplitudes depend explicitly on time, consistent with a wave packet approach. We investigate the phase shifts and amplitude ratios between the GW components, which include the horizontal (u'_H) and vertical (w') velocity, density (ρ'), pressure (p'), and temperature (T') perturbations. We show how GWs with large vertical wavelengths λ_z have dramatically different phase and amplitude relations than those with small λ_z. For zero viscosity, as $|\lambda_z|$ increases, the phase between u'_H and w' decreases from 0 to $\sim -90°$, the phase between u'_H and T' decreases from ~ 90 to $0°$, and the phase between T' and ρ' decreases from ~ 180 to $0°$ for $\lambda_H \gg |\lambda_z|$, where λ_H is the horizontal wavelength. This effect lessens substantially with increasing altitudes, primarily because the density scale height $\mathcal{H}$ increases. We show how in-situ satellite measurements of either (1) the 3D neutral wind or (2) ρ', T', w', and the cross-track wind, can be used to infer a GW's λ_H, λ_z, propagation direction, and intrinsic frequency ω_{Ir}. We apply this theory to a GW observed by the DE2 satellite. We find a significant region of overlap in parameter space for 5 independent constraints (i.e., T'_0/ρ'_0, the phase shift between T' and w', and the distance between wave crests), which provides a good test and validation of this theory. In a companion paper, we apply this theory to ground-based observations of a GW over Alaska.

Citation: Vadas, S. L., and M. J. Nicolls (2012), The phases and amplitudes of gravity waves propagating and dissipating in the thermosphere: Theory, *J. Geophys. Res.*, *117*, A05322, doi:10.1029/2011JA017426.

1. Introduction

[2] GWs are ubiquitous in the thermosphere [e.g., *Djuth et al.*, 1997, 2004; *Oliver et al.*, 1997]. Increasing observational and modeling evidence suggests that some GWs generated in the lower atmosphere (e.g., from deep convection, mountain wave breaking) may propagate into the thermosphere [*Bauer*, 1958; *Georges*, 1968; *Röttger*, 1977; *Hung and Kuo*, 1978; *Waldock and Jones*, 1987; *Kelley*, 1997; *Hocke and Tsuda*, 2001; *Bishop et al.*, 2006; *Vadas and Nicolls*, 2009], where they eventually dissipate [*Pitteway and Hines*, 1963; *Francis*, 1973; *Richmond*, 1978]. The momentum deposited during GW dissipation excites secondary GWs [*Vadas and Liu*, 2009, 2011] which can propagate to z = 300–500 km before dissipating [*Vadas*, 2007]. GWs are also excited at high latitudes by Joule heating, particle precipitation, and the Lorentz forcing which accompanies the rapidly evolving aurora [*Chimonas and Hines*, 1970; *Chimonas and Peltier*, 1970; *Francis*, 1975; *Hunsucker*, 1982; *Mayr et al.*, 1990; *Hocke and Schlegel*, 1996]. These GWs can also propagate to z = 300–500 km before dissipating [*Richmond*, 1978; *Hajkowicz*, 1990; *Tsugawa et al.*, 2003; *Bruinsma and Forbes*, 2009].

[3] A GW causes periodic oscillations (in space and time) of the constituent species of the fluid in the thermosphere, such as O and N_2 [*DelGenio and Schubert*, 1979; *Gross et al.*, 1984]. It also creates phase-shifted oscillations in the plasma [*Klostermeyer*, 1972; *Gross et al.*, 1984; *Hocke et al.*, 1996; *Earle et al.*, 2008]. When one constituent species dominates (typically above 200 km altitude), the fluid can be considered as a "single-species". This is the situation we consider in this paper. Then, the sinusoidal, periodic oscillations of a GW occurs in all of the fluid perturbations, namely the horizontal and vertical velocities, temperature, density, and pressure. While each of these neutral fluid components oscillates at the same frequency and horizontal/vertical wave numbers [*Einaudi and Hines*, 1970], they are phase-shifted from each other. For GWs with $|\lambda_z| < \mathcal{H}$, (i.e., the Boussinesq approximation), the phase shifts between the GW components are straightforward. For example, the zonal u' and vertical w' velocities are in phase for an eastward-propagating GW, while the density ρ' and temperature T' perturbations are 180° out of

[1]CORA Division, Northwest Research Associates, Inc., Boulder, Colorado, USA.
[2]Center for Geospace Studies, SRI International, Menlo Park, California, USA.

Corresponding author: S. L. Vadas, CORA Division, Northwest Research Associates, Inc., 3380 S. Mitchell Ln., Boulder, CO 80301, USA. (vasha@co-ra.com)

0148-0227/12/2011JA017426

phase [*Fritts and Alexander*, 2003]. Such GWs with small $|\lambda_z|$ dissipate at z < 130 km [*Djuth et al.*, 1997, 2004; *Oliver et al.*, 1997; *Midgley and Liemohn*, 1966; *Vadas*, 2007]. At higher altitudes, $|\lambda_z| \gg \mathcal{H}$, so the Boussinesq approximation is not valid. As shown in this paper, as $|\lambda_z|$ increases, the phase shift between u' and w' increases significantly, while the phase shift between ρ' and T' decreases significantly. This is due to the increasing importance of the pressure perturbation. Additionally, the amplitude ratios of these GW components depend sensitively and uniquely on λ_H, λ_z, and the GW's intrinsic frequency ω_{Ir}. Finally, we find that both the phase shifts and amplitude ratios depend sensitively on the kinematic viscosity ν.

[4] *Gross et al.* [1984] used the phase shifts and amplitude ratios of the O and N_2 fluctuations to estimate the direction of propagation (within 180°) for a spectrum of GWs observed by the AE-C satellite. Their theory was non-viscous, however, and might have been a factor in their having difficulty finding overlapping, compatible solutions. *Innis and Conde* [2002, hereinafter IC02] utilized the phases of GWs to determine the propagation directions of GWs to within 90°. They did this by analyzing in-situ, high-latitude, DE2 satellite measurements of w', the cross-track velocity u'_{track}, the inferred height change (h), and the inferred pressure p'. For example, if u'_{track} was in phase with p', then the wave propagated eastward. And if h led w' by 90°, then the spacecraft was traveling in the same direction as the GW. In this way, IC02 could infer a GW's propagation direction to within 90°. ω_{Ir} was determined via $h = w'/i\omega_{Ir}$. Although IC02 took into account fluid compressibility (i.e., non-negligible pressure perturbations), they did not take into account viscous dissipation. And as we show in this paper, it is possible to use the specific amount of phase shifting between the GW components (i.e., between w', u'_{track}, ρ', and T'), as well as their corresponding amplitude ratios (i.e., $(\rho'_0/\bar{\rho})/w'_0$), to gain a much more accurate estimate of the GW propagation direction. This procedure, which involves the use of the dissipative polarization and dispersion relations, also yields λ_H, λ_z, and ω_{Ir}. These relations are derived in this paper under the assumptions that (1) the source of the GW is spatially and temporally localized, (2) the GW is linear, and (3) $|\lambda_z| < 4\pi\mathcal{H}$ if the GW is dissipating.

[5] No theory should be assumed "correct", however, without testing and validation (if possible) within well-defined limits. Therefore, we also apply our derived relations to several observed GWs. We provide two "tests" of this theory in this and in our companion paper. In this paper, we compare the phases and amplitude ratios of w', u'_{track}, ρ', and T' for a GW reported by IC02 with this theory, and show that the range of inferred λ_H and λ_z overlap well with each other. Our second (more substantial) "test" is contained in our companion paper. Recently, high-resolution, 3D neutral wind and temperature measurements using Fabry Perot observatories in Alaska have determined the phase shifts and amplitude ratios of a monochromatic GW observed there on 9–10 January 2010 [*Nicolls et al.*, 2012]. Using forward modeling, λ_H and the direction of propagation were determined. Accompanying Poker Flat Incoherent Scatter Radar (PFISR) measurements determined a reasonable range for λ_z. We compared these results with this theory, and found reasonably good agreement.

[6] *Vadas and Fritts* [2005, hereinafter VF05] originally derived the dissipative polarization and dispersion relations for high-frequency GWs undergoing dissipation with the assumptions listed above (see equations (B1)–(B4) in VF05). Because they were interested in an anelastic approximation, however, they neglected a potentially important dissipative divergence term. We include this term here, and derive the full compressible polarization relations for high-frequency GWs and AWs which dissipate from kinematic viscosity and thermal diffusivity in the thermosphere (section 2). In order to justify our wave packet approach, we assume that these GWs are from time-dependent and spatially localized wave sources. In section 3, we show how the GW phase shifts and amplitude ratios depend on λ_H and λ_z, as well as on the background temperature, viscosity, and buoyancy period. Section 4 shows how a GW's ω_{Ir}, direction of propagation, and 3D wave vector can be uniquely and simply determined from this theory using in-situ satellite measurements of (1) the 3D velocity vector (u', v', w') or (2) ρ', T', w', and u'_{track}. We also apply this theory to a GW observed by DE2 in section 4. Section 5 contains our conclusions. A companion paper compares the predictions of this theory with Fabry-Perot observations of a monochromatic GW observed in the thermosphere above Alaska on 9–10 January 2010 [*Nicolls et al.*, 2012].

2. Dissipative Dispersion and Polarization Relations for High-Frequency Gravity Waves and Acoustic Waves

2.1. Navier Stokes Fluid Equations

[7] We utilize the compressible Navier Stokes fluid equations to describe the propagation and dissipation of high-frequency GWs in the thermosphere. Here, we define a high-frequency wave to be a GW or AW with a period less than a few hours. We also assume the fluid can be approximated as a single species, which is a reasonable assumption above 200 km altitude. The momentum, heat, and mass conservation equations, respectively, are [*Kundu*, 1990]

$$\frac{D\mathbf{v}_i}{Dt} = -\frac{RT}{\rho}\frac{\partial\rho}{\partial x_i} - R\frac{\partial T}{\partial x_i} + \mathbf{g}\delta_{i3} + \frac{1}{\rho}\frac{\partial}{\partial x_j} \cdot \left[\mu\left(\frac{\partial \mathbf{v}'_i}{\partial x_j} + \mathrm{a}\frac{\partial \mathbf{v}'_j}{\partial x_i} - \frac{2\mathrm{a}}{3}(\nabla.\mathbf{v}')\delta_{ij}\right)\right] \tag{1}$$

$$\frac{DT}{Dt} = -(\gamma-1)T\nabla\cdot\mathbf{v} + \frac{\gamma}{\rho}\frac{\partial}{\partial x_j}\left(\frac{\mu}{\mathrm{Pr}}\frac{\partial T'}{\partial x_j}\right) \tag{2}$$

$$\frac{D\rho}{Dt} = -\rho\nabla.\mathbf{v}, \tag{3}$$

where $\mathbf{v} = (u, v, w)$ is velocity (in x, y, and z geographic coordinates), ρ is density, T is temperature, $\mathbf{g} = -g\hat{z}$ is gravitational acceleration, μ is molecular viscosity, C_p (C_V) is heat capacity at constant pressure (volume), $\gamma/(\gamma-1) \equiv C_p/\mathrm{R}$, $\mathrm{R} = 8308/\mathrm{X_{MW}}$ m^2 s^{-2} K^{-1}, $\gamma = C_p/C_v$, $\mathrm{X_{MW}}$ is mean molecular weight of the particle in the gas, Pr is Prandtl number, $D/Dt = \partial/\partial t + \mathbf{v}.\nabla$, and primes denote perturbation quantities. The subscript "i" denotes the ith component, and repeated indices imply summation over j = 1, 2, 3. The notation section lists many of the symbols used in this paper. Following VF05, we have written the equations in a form that eliminates the pressure and potential temperature. We neglect wave-induced diffusion and the Coriolis force, since we are only interested in describing the dissipation of high-frequency GWs with periods less than a few hours. Thus, these equations are applicable at all latitudes under our specified assumptions. We also neglect ion drag, which is unimportant for high-frequency, nighttime GWs, but may be important for daytime GWs when ion densities are large [*Yeh et al.*, 1975]. We insert the variable "a" in front of the compressible divergence terms in equation (1), because these were the dissipative terms neglected in VF05; a = 1 includes these new terms, while a = 0 neglects these terms and yields the VF05 results.

2.2. Linearized Navier Stokes Fluid Equations

[8] We first consider an internal wave packet propagating in the $x - z$ plane. (We will generalize to 3D shortly.) Linearizing equations (1)–(3), we obtain

$$u'_t = -w'\frac{d\bar{U}}{dz} - RT'_x - \frac{c_s^2}{\gamma\bar{\rho}}\rho'_x + \nu\left(\nabla^2 u' + \frac{\mathrm{a}}{3}(u'_x + w'_z)_x\right) + \frac{1}{\bar{\rho}}\frac{d\mu}{dz}(u'_z + \mathrm{a}w'_x) \quad (4)$$

$$w'_t = -RT'_z - \frac{c_s^2}{\gamma\bar{\rho}}\rho'_z + \frac{c_s^2}{\gamma\mathcal{H}}\left(\frac{T'}{\bar{T}} - \frac{\rho'}{\bar{\rho}}\right) + \nu\left(\nabla^2 w' + \frac{\mathrm{a}}{3}(u'_x + w'_z)_z\right) + \frac{1}{\bar{\rho}}\frac{d\mu}{dz}\left(\left(1 + \frac{1}{3}\mathrm{a}\right)w'_z - \frac{2}{3}\mathrm{a}u'_x\right) \quad (5)$$

$$T'_t = -w'\frac{d\bar{T}}{dz} - (\gamma - 1)\bar{T}(u'_x + w'_z) + \frac{\gamma\nu}{\mathrm{Pr}}\nabla^2 T' + \frac{\gamma}{\mathrm{Pr}\bar{\rho}}\frac{d\mu}{dz}T'_z \quad (6)$$

$$\rho'_t = \frac{\bar{\rho}}{\mathcal{H}}w' - \bar{\rho}(u'_x + w'_z), \quad (7)$$

where $\mathcal{H} = -\bar{\rho}/(d\bar{\rho}/dz)$ is density scale height, $c_s \equiv \sqrt{\gamma R\overline{T}}$ is speed of sound, and $\nu = \mu/\bar{\rho}$ is kinematic viscosity. The hydrostatic equation is $-(\mathrm{R}\overline{T}/\bar{\rho})d\bar{\rho}/dz - g - \mathrm{R}d\overline{T}/dz = 0$, or $\mathrm{R}\overline{T}/\mathcal{H} = g + \mathrm{R}d\overline{T}/dz$. The subscripts t, x, and z represent $\partial/\partial t + \overline{U}\partial/\partial x$, $\partial/\partial x$, and $\partial/\partial z$, respectively, and the overlines denote the unperturbed values. Equations (4)–(7) are the general linearized Navier Stokes fluid equations.

[9] We factor out a wave's increasing amplitude with altitude [*Pitteway and Hines*, 1963],

$$\tilde{u} = \left(\frac{\bar{\rho}}{\rho_0}\right)^{1/2} u', \quad \tilde{w} = \left(\frac{\bar{\rho}}{\rho_0}\right)^{1/2} w', \quad \tilde{T} = \left(\frac{\bar{\rho}}{\rho_0}\right)^{1/2} T', \quad \tilde{\rho} = \left(\frac{\rho_0}{\bar{\rho}}\right)^{1/2}\rho', \quad (8)$$

where ρ_0 is the density at z = 0. Within a wave packet, the wavelength and period are quasi-sinusoidal, and therefore vary with distance and time. If the variation at a single location and time can be approximated as sinusoidal, then local wave parameters (such as horizontal wavelength, period, etc) can be determined [*Lighthill*, 1978]. The local dispersion and polarization relations can then be determined at this location and time. Following *Lighthill* [1978], we assume solutions of the form

$$\tilde{u} = \tilde{u}_0(x, z, t)\exp[i\xi(x, z, t)], \quad (9)$$

where $\xi(x, z, t)$ is the local wave phase, $\partial\xi/\partial x = k$, $\partial\xi/\partial z = m$, $\partial\xi/\partial t = -\omega$, ω is the observed wave frequency, and $\mathbf{k} = (k, l, m)$ is the local wave number vector in geographic coordinates. (Note that if the wave is monochromatic in space and time, the phase is $\xi = kx + mz - \omega t$.) In order to obtain an analytic solution from equations (4)–(7), we assume that the background temperature, horizontal wind components, and kinematic viscosity are *locally* constant. This latter condition only applies over the altitude range where the wave is dissipating (i.e., where ν is important), and is a good approximation if $|\lambda_z| < 4\pi\mathcal{H}$ at the dissipation altitude. Here, $\lambda_x = 2\pi/k$, $\lambda_y = 2\pi/l$, $\lambda_z = 2\pi/m$ are the zonal, meridional and vertical wavelengths, respectively. Equations (4)–(5) contain terms proportional to $\frac{1}{\bar{\rho}}(d\mu/dz)$. Although μ depends weakly on the temperature, $\mu \propto \overline{T}^{0.71}$ [*Dalgarno and Smith*, 1962], we neglect the $\frac{1}{\bar{\rho}}(d\mu/dz)$ terms because $\overline{T}$ is assumed locally constant. (Note that $\overline{T} \sim$ *constant* for z > 200–220 km because of the very large thermal conductivity that occurs in that region of the thermosphere.) We also assume a constant Prandtl number of Pr = 0.7 [*Kundu*, 1990], and thus ignore its slight variation with temperature [*Yeh et al.*, 1975]. Note that the viscosity ($\propto \mu$) and thermal conductivity ($\propto \mu$/Pr) have comparable damping effects on the GWs or AWs.

[10] We generalize to wave propagation in 3D by substituting $k_H{}^2 = k^2 + l^2$ for k^2, and the intrinsic frequency

$$\omega_I = \omega - k\overline{U} - l\overline{V} \quad (10)$$

for $\omega - k\overline{U}$, and the horizontal velocity perturbation (along the direction of GW propagation) $\widetilde{u_{H0}}$ in for $\tilde{u}_0$. Equations (4)–(7) can then be solved analytically for $\widetilde{u_{H0}}$, $\tilde{w}_0$, etc.

2.3. Wave Packet Approach for Time-Dependent, Spatially Localized Wave Sources

[11] We assume here that the intrinsic frequency, ω_I, is complex, and can be written as a sum of real and imaginary parts (VF05):

$$\omega_I = \omega_{Ir} + i\omega_{Ii}. \quad (11)$$

This solution ansatz assumes that the vertical wave number m is real and the ground-based frequency ω is complex [*Vadas*, 2007; *Vadas and Nicolls*, 2008, 2009; *Vadas and Fritts*, 2009], rather than the "full-wave", steady state solution ansatz which assumes that m is complex and $\omega = \omega_r$ is real [e.g., *Pitteway and Hines*, 1963; *Volland*, 1969b; *Francis*, 1973; *Yeh and Liu*, 1974; *Yeh et al.*, 1975; *Hickey and Cole*, 1987; *Walterscheid and Hickey*, 2011]. Here, ω_r is the real part of the ground-based frequency ω. The complex-ω_I ansatz results in wave solutions that depend explicitly on time. They can therefore describe the propagation and dissipation of waves excited by time-dependent, spatially localized wave sources in a straightforward manner. However, summations of well-posed, real-ω_I solutions (in a Fourier series) can also yield time-dependent wave solutions [e.g., *Salby and Garcia*, 1987; *Vadas and Fritts*, 2001, 2009]. *Hickey et al.* [2000, 2009] employ real-ω_I, steady state solutions to study transient gravity wave packets; however, it is unclear if such a sum yields accurate solutions (in z, λ_z) to the time-dependent Navier Stokes equations.

[12] The full wave model solutions shown in *Walterscheid and Hickey* [2011] essentially solve equations (4)–(7) numerically, but with the boundary conditions that the wave source is steady state (i.e., does not vary in time) and is horizontally uniform (i.e., does not vary in x and y). These conditions are quite restrictive. As emphasized by *Walterscheid and Hickey* [2011], for zero background wind, this steady state solution results in $|\lambda_z|$ increasing exponentially in z above the altitude where the GW's amplitude is maximum (dubbed its dissipation altitude, or $z_{\rm diss}$). This result, that λ_z increases as a result of dissipation, is a general result of full wave models [e.g., *Pitteway and Hines*, 1963; *Volland*, 1969b; *Francis*, 1973; *Yeh and Liu*, 1974; *Yeh et al.*, 1975; *Hickey and Cole*, 1987]. We note that $|\lambda_z|$ asymptotes to a constant value at sufficiently great heights in full wave models, unless opposed by wind effects (M. Hickey, personal communication, 2012). The exponential increase of $|\lambda_z|$ was demonstrated for GWs with small vertical wavelengths of $|\lambda_z| \ll 4\pi\mathcal{H}$ in *Walterscheid and Hickey* [2011]. In contrast, the wave packet solution derived in VF05 (and re-derived here with additional terms proportional to a) assumes that the wave source is time-dependent and spatially localized. This latter solution results in the GW's $|\lambda_z|$ remaining constant or decreasing/increasing slightly with altitude above $z_{\rm diss}$, depending on whether $\overline{T}$ is constant or is increasing at $z_{\rm diss}$ (see section 3 for several examples). This occurs even for GWs with $|\lambda_z| \ll 4\pi\mathcal{H}$, for which the "$\nu$-locally constant" assumption is completely justified.

[13] The radically different behavior of λ_z with altitude shows that the time-dependent solutions are fundamentally different from the steady state solutions. We can understand this difference as follows. Molecular viscosity is the transfer of momentum which occurs during molecular collisions. In a dense fluid, ν is small because collisions are frequent and the distance between collisions is small. In a rarified fluid (i.e., $\bar{\rho}$ small), ν is much larger because the distance between infrequent collisions is much larger, thereby enabling a significant transfer of momentum over much larger distances. However, the trajectories of molecules (after collisions) are significantly skewed from their original direction of motion. These skew directions can damp a GW, because the fluid motion needs to follow ellipses in order to maintain a GW. Molecular motion in all directions is damped equally if ν is constant. However, since viscosity increases (and $\bar{\rho}$ decreases) exponentially in z, those molecules with larger vertical motions experience less collisions, more skewed trajectories (after collisions), and more damping than those molecules with smaller vertical motions. The resulting coherent portion of the ellipses becomes shortened or "squashed" in z. This is manifested physically by the wave packet refracting toward the horizontal direction as it dissipates, with $|\lambda_z|$ decreasing. In a steady state flow, new GWs are continuously adding upward momentum to the fluid where wave dissipation is occurring. This momentum is transferred to the fluid, thereby causing the ellipses to lengthen in z. This is manifested physically as $|\lambda_z|$ increasing for the resulting wave pattern. This increase in $|\lambda_z|$ causes steady state GWs to penetrate deeper into the thermosphere than a single wave packet (with the same ω_r and λ_H). We speculate that if a time-dependent numerical simulation is run with a continuous generation of upward-propagating GWs at the lower boundary, $|\lambda_z|$ (at $z_{\rm diss}$) and the wave dissipation altitude will slowly increase in time as the solution transitions from a dissipating wave packet to a steady state solution.

[14] One of the main criticisms that *Walterscheid and Hickey* [2011] made of the wave packet (ray trace) approach in VF05 was that the vertical group velocity c_{gz} did not equal the "signal" velocity $w_s = -\omega_r/m$ above $z_{\rm diss}$. There are 2 problems with that comparison. First, those authors plotted $w_s = -\omega_r/m$ from the steady state solution (FW), and c_{gz} from the wave packet (ray trace) solution; since they are fundamentally different solutions, one should not expect them to agree. Second, w_s is the negative of the vertical phase velocity of a GW, $c_z \equiv \omega_r/m$. It is well-known that the energy in a GW packet moves (in the vertical direction) at the vertical group velocity, not at the vertical phase velocity [*Yeh and Liu*, 1974; *Lighthill*, 1978]. Therefore, w_s is not relevant for describing the vertical velocity of the wave packet as it propagates and dissipates in the thermosphere. Even so, we show in section 3.3 that if we plot c_{gz} versus $-\omega_r/m$ for our wave packet solution for a GW similar to that shown in *Walterscheid and Hickey* [2011], they are within 8% up to $z_{\rm diss}$, and are within 20% at an altitude where the momentum fluxes are negligible.

[15] An important question to ask is whether nature typically sends GWs into the thermosphere from steady state, spatially uniform sources, or from time-dependent, spatially localized sources. Because $|\lambda_z|$ increases exponentially with z for steady state solutions, using these solutions for time-dependent wave sources likely results in GWs penetrating too high in the thermosphere, thereby greatly increasing their amplitudes and resulting effects artificially as compared to their smaller increase and lower dissipation altitudes if more appropriate time-dependent solutions had been used instead.

[16] In order to answer the question as to which solution type (steady state or wave packet) is most appropriate for modeling the propagation and dissipation of GWs in the thermosphere, it is important to understand the GW source one wishes to model. Commonly modeled GW sources such as deep convection, wave-breaking, auroral heating, and tsunamis are all highly time-dependent, spatially localized GW sources, and therefore should be modeled with the wave packet solutions rather than the steady state, full wave solutions. In order to model the propagation and dissipation of GWs in the thermosphere from unknown sources, we first must determine which solution type agrees best with the observations. As is well-known, $|\lambda_z|$ increases exponentially with altitude in the thermosphere for a white-noise or convective *spectrum* of (many) GWs using the time-dependent, spatially localized, wave packet solutions [*Vadas*, 2007]. This is because of dissipative filtering. Therefore, for both the steady state and wave packet solutions, $|\lambda_z|$ increases exponentially with altitude for a *spectrum of GWs*. In order to distinguish between these solutions observationally, then,

one must look for measurements of λ_z as a function of altitude for individual GWs. Such individual-GW observations now exist. GW observations in Alaska using PFISR [*Vadas and Nicolls*, 2009, Figures 8 and 17] and observations in Puerto Rico using the Arecibo Observatory [*Djuth et al.*, 2010, Figure 15] both show that for individual GWs, λ_z remains approximately constant or decreases/increases slightly with altitude above $z_{\rm diss}$ for nearly all of the GWs. Recent Arecibo Observatory observations of a few dozen GWs confirms this conclusion, and shows that λ_z rarely increases exponentially with z above $z_{\rm diss}$ (S. L. Vadas and M. J. Nicolls, manuscript in preparation, 2012). Therefore, the GWs most commonly observed in the thermosphere most likely arise from time-dependent, spatially localized sources, rather than from steady state, horizontally uniform sources. Here, by thermospheric "source", we refer to the original GW source plus any time or spatially dependent wind-filtering which takes place between the original source and the observation location.

2.4. Dissipative, Compressible GW and AW Dispersion and Polarization Relations for Time-Dependent, Spatially Localized Wave Sources

[17] Substituting equations (8)–(10) into equations (4)–(7), straightforward and tedious algebra yields the compressible, complex, dispersion relation for AWs and GWs damped by molecular viscosity and thermal diffusivity:

$$-\frac{\omega_I}{c_s^2}\left(\omega_I-\frac{i\gamma\alpha\nu}{\rm Pr}\right)(\omega_I-i\alpha\nu)\left(\omega_I-i\alpha\nu\left(1+\frac{\rm a}{3}\right)\right)+(\omega_I-i\alpha\nu)\cdot\left(\omega_I-\frac{i\alpha\nu}{\rm Pr}\right)\left(\mathbf{k}^2+\frac{1}{4\mathcal{H}^2}\right)=k_H{}^2N_B{}^2, \quad (12)$$

where $\mathbf{k}^2=k_H^2+m^2$, $k_H^2=k^2+l^2$, and

$$\alpha\equiv-\mathbf{k}^2+\frac{1}{4\mathcal{H}^2}+\frac{im}{\mathcal{H}}. \quad (13)$$

Additionally, $N_B{}^2=(\gamma-1)c_s^2/\left(\gamma^2\mathcal{H}^2\right)=(\gamma-1)g^2/\left(\gamma R\overline{T}\right)$ is buoyancy frequency squared and $\mathcal{H}={\rm R}\overline{T}/g$ for this isothermal approximation (i.e., $\overline{T}=constant$). (The non-isothermal expression is $N_B{}^2\equiv\left(g/\overline{\theta}\right)d\overline{\theta}/dz=\left(g/\overline{T}\right)\left(d\overline{T}/dz+g/C_p\right)$, where $\theta=T(p_s/p)^{(\gamma-1)/\gamma}$ is potential temperature and p_s is standard pressure.) We note that equation (12) agrees with equation (19) in VF05 for a = 0. In the limit that the viscosity is zero, equation (12) becomes

$$\omega_{Ir}^4-c_s^2\left(\mathbf{k}^2+1/4\mathcal{H}^2\right)\omega_{Ir}^2+c_s^2k_H{}^2N_B{}^2=0, \quad (14)$$

which is the well-known non-dissipative compressible dispersion relation [*Hines*, 1960].

[18] The solutions to equation (12) are complicated. Two are up- and down-going AWs and GWs, two are up- and down-going heat conduction waves, and four are up- and down-going ordinary and extraordinary viscous waves [*Midgley and Liemohn*, 1966; *Volland*, 1969a; *Yeh and Liu*, 1974; *Maeda*, 1985; *Hickey and Cole*, 1987]. Here, we are only interested in the GW and AW solutions. GWs have frequencies smaller than N_B, while AWs have frequencies larger than N_B [*Hines*, 1960]. However, we should note that viscous and heat conduction waves can become important above $z_{\rm diss}$.

[19] In solving equations (4)–(7), we also obtain the compressible, dissipative polarization relations for GWs and AWs:

$$\widetilde{u_H}_0=\frac{\gamma}{ik_Hc_s^2\mathcal{D}}\left[i\omega_I\left(i\omega_I+\frac{\gamma\alpha\nu}{\rm Pr}\right)\left(i\omega_I+\nu\left(\alpha+\frac{\rm a}{3}\left(\alpha+k_H{}^2\right)\right)\right)+c_s^2\left(m^2+\frac{1}{4\mathcal{H}^2}\right)\left(i\omega_I+\frac{\alpha\nu}{\rm Pr}\right)\right]\widetilde{w}_0 \quad (15)$$

$$\widetilde{T}_0=\frac{(\gamma-1)\overline{T}}{c_s^2\mathcal{D}}\left[\gamma i\omega_I(i\omega_I+\alpha\nu)+\frac{c_s^2}{\mathcal{H}}\left(im+\frac{1}{2\mathcal{H}}\right)\right]\widetilde{w}_0 \quad (16)$$

$$\widetilde{\rho}_0=\frac{\rho_0}{c_s^2\mathcal{D}}\left[\gamma\left(i\omega_I+\frac{\gamma\alpha\nu}{\rm Pr}\right)\left(i\omega_I+\nu\left(\alpha+\frac{\rm a}{3\mathcal{H}}\left(im+\frac{1}{2\mathcal{H}}\right)\right)\right)-\frac{(\gamma-1)c_s^2}{\mathcal{H}}\left(im-\frac{1}{2\mathcal{H}}\right)\right]\widetilde{w}_0, \quad (17)$$

where $\widetilde{u_H}$ is the GW or AW horizontal velocity along the direction of wave propagation, and

$$\mathcal{D}=\left[i\omega_I\left(\gamma im+\frac{1}{\mathcal{H}}-\frac{\gamma}{2\mathcal{H}}-{\rm b}\right)+\frac{\gamma\alpha\nu}{\rm Pr}\left(im+\frac{1}{2\mathcal{H}}-{\rm b}\right)\right], \quad (18)$$

$${\rm b}=\frac{i{\rm a}\nu\gamma\omega_I}{3c_s^2}\left(im+\frac{1}{2\mathcal{H}}\right). \quad (19)$$

For these high-frequency gravity and acoustic waves, the zonal and meridional perturbation velocities are then

$$\tilde{u}=\frac{k}{k_H}\widetilde{u_H},\quad \tilde{v}=\frac{l}{k_H}\widetilde{u_H}. \quad (20)$$

(Although VF05 states that "$\tilde{v}_0$ can be obtained trivially by replacing $k\rightarrow l$ in equation (B1)", this is not the correct way to generalize those results to 3D. This mistake was corrected in equation (58) of *Vadas and Fritts* [2009]. The correct expressions are shown here in equations (15) and (20).) Equations (15)–(17) agree with equations (B1)–(B3) in VF05 for a = 0. For all of the non ray-trace figures shown in this paper, we set a = 1.

[20] Although the dispersion and polarization relations derived in this section apply to both high-frequency GWs and AWs (i.e., with periods less than a few hours), we now apply these results only to GWs in sections 3 and 4. This is because GWs tend to be far more prevalent than AWs in the thermosphere. However, these relations can also be used for future thermospheric studies of AWs.

3. Phase Shifts and Amplitude Ratios of the GW Components

3.1. Non-dissipating GWs

[21] We first discuss how compressibility affects the phase shifts and amplitude ratios of the various components of non-dissipating GWs. Comparing $\mathbf{k}^2\sim m^2$ with $1/4\mathcal{H}^2$ from the non-dissipative dispersion relation shown in

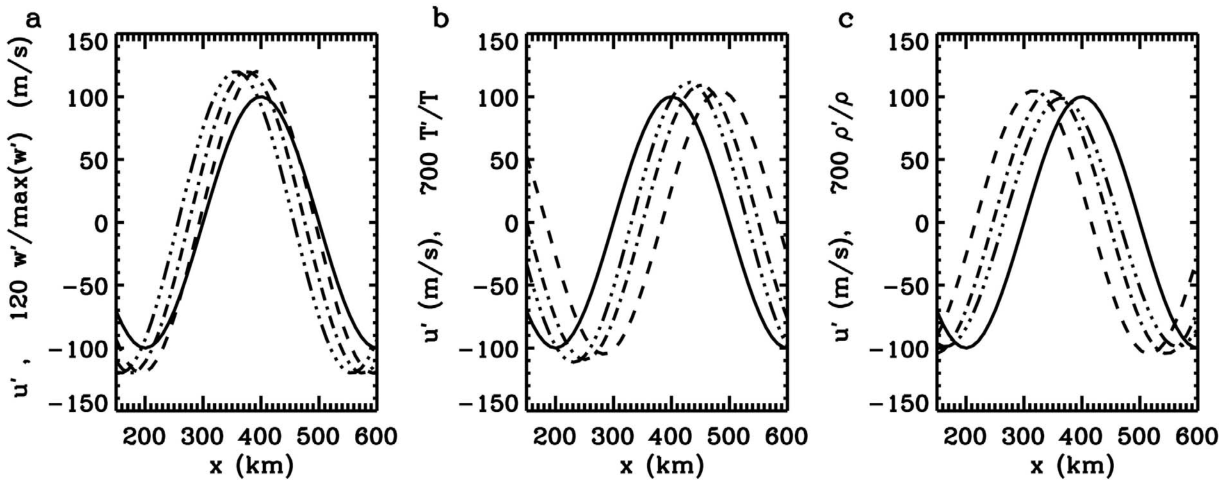

Figure 1. Velocity, density, and temperature perturbations for non-dissipating, eastward-propagating GWs with $\lambda_x = 400$ km, $l = 0$, and $\nu = 0$. Solid lines show $\tilde{u}$. Dash, dash-dot, and dash-dot-dot-dot lines show $\lambda_z = -50$, -200, and -400 km, respectively. (a) 120 $\tilde{w}/\tilde{w}_0$. $\tilde{w}_0$ is 12, 25, and 23 m/s for $\lambda_z = -50$, -200, and -400 km, respectively. (b) $700\widetilde{T}/\overline{T}$. (c) $700\widetilde{\rho}/\overline{\rho}$.

equation (14), we see that compressible effects are expected to be important for $|\lambda_z| > 2\pi\mathcal{H}$. GWs which can propagate to the mid or upper-thermosphere before dissipating must have relatively large vertical wavelengths [*Hines*, 1964; *Vadas*, 2007]. Therefore, we expect compressible effects to be important for those GWs which can propagate to the mid or upper-thermosphere before dissipating.

[22] Figure 1 shows a snapshot in time of upward and eastward-propagating GWs as a function of x in a non-dissipative ($\mu = 0$) atmosphere with $\lambda_x = 400$ km, and $\lambda_z = -50$, -200, and -400 km. From equation (9), increasing time (for a fixed x) implies decreasing x (for a fixed t). Here, we choose lower thermospheric values of $\mathcal{H} = 15$ km, $\gamma = 1.45$ and $g = 9.4$ m^2/s, so that $2\pi\mathcal{H} = 94$ km. Additionally, we use the isothermal expressions $c_s = \sqrt{\gamma g \mathcal{H}}$ and $N_B = \sqrt{(\gamma-1)g^2/c_s^2}$. (Here, $c_s = 450$ m/s and $\tau_B = 2\pi/N_B = 8$ min.) For simplicity, we choose $\overline{U} = \overline{V} = 0$. The magnitude of $\tilde{u}$ is set to be $\tilde{u}_0 = 100$ m/s for all GWs. Here, the subscript "0" on a fluid variable indicates its amplitude. Figure 1a shows the vertical velocity perturbations normalized to 120 m/s in order to more easily see the differences between the solutions. For small $|\lambda_z|$, $\tilde{u}$ and $\tilde{w}$ are nearly in phase, as expected [*Fritts and Alexander*, 2003]. For $|\lambda_z| > 2\pi\mathcal{H}$, $\tilde{w}$ and $\tilde{u}$ are significantly phase-shifted. For $\lambda_z = -400$ km, $\tilde{u}$ leads $\tilde{w}$ by $\sim$45°. Figures 1b and 1c show the temperature and density perturbations, respectively, for the same GWs. Although $\tilde{u}$ and $\tilde{T}$ are 90° out of phase for small $|\lambda_z|$, this shift decreases as $|\lambda_z|$ increases. Similarly, the phase shift between $\tilde{u}$ and $\tilde{\rho}$ decreases as $|\lambda_z|$ increases. For small $|\lambda_z|$, the density and temperature are 180° out of phase; this shift decreases substantially as $|\lambda_z|$ increases. Note that while $\tilde{w}_0/\tilde{u}_0$ depends sensitively on λ_z (see values in figure caption), $\tilde{T}_0/\tilde{u}_0$ and $\tilde{\rho}_0/\tilde{u}_0$ do not depend significantly on λ_z.

3.2. Dissipating GWs

[23] Next we discuss how dissipation affects the phase shifts and amplitude ratios of the GW components. We choose $\mathcal{H} = 30$ km, $\gamma = 1.6$, and $\overline{U} = \overline{V} = 0$. Additionally, we use the isothermal expressions $c_s = \sqrt{\gamma g \mathcal{H}}$ and $N_B = \sqrt{(\gamma-1)g^2/c_s^2}$. When $\nu \neq 0$, we determine ω_I from equation (12) carefully in order to avoid the viscous and heat conduction waves. We first neglect the $1/c_s^2$ terms and solve the resulting quadratic equation analytically for ω_I:

$$(\omega_I - i\alpha\nu)\left(\omega_I - \frac{i\alpha\nu}{\mathrm{Pr}}\right)\left(\mathbf{k}^2 + \frac{1}{4\mathcal{H}^2}\right) - k_H{}^2 N_B{}^2 = 0. \qquad (21)$$

This yields the anelastic solution for an upward-propagating GW with $|\lambda_z| < 4\pi\mathcal{H}$. (This solution, with Pr = 1, was discussed at length in sections 4 and 5 of VF05). We then rearrange equation (12), and substitute ω_I from equation (21) (or from the previous iteration) into the square bracket in the following equation:

$$(\omega_I - i\alpha\nu)\left(\omega_I - \frac{i\alpha\nu}{\mathrm{Pr}}\right)\left(\mathbf{k}^2 + \frac{1}{4\mathcal{H}^2}\right) - \left[k_H{}^2 N_B{}^2 + \frac{\omega_I}{c_s^2}\left(\omega_I - \frac{i\gamma\alpha\nu}{\mathrm{Pr}}\right)\right.$$
$$\left.\cdot\,(\omega_I - i\alpha\nu)\left(\omega_I - i\alpha\nu\left(1 + \frac{\mathrm{a}}{3}\right)\right)\right] = 0. \qquad (22)$$

We then solve equation (22) as a quadratic equation for ω_I. We repeat this procedure several times until the solution converges. Finally, we solve equation (12) using Newton's method. This procedure for determining ω_I is used for all of the solutions in this paper.

[24] Figure 2 shows snapshots of $\tilde{u}$, $\tilde{w}$, $\tilde{T}$, and $\tilde{\rho}$ as a function of x for upward and eastward-propagating, medium-scale GWs. Here, we choose $\mathcal{H} = 30$ km, $\gamma = 1.6$ and $g = 9.1$ m^2/s, and $\overline{U} = \overline{V} = 0$ for simplicity. (Here, $c_s = 660$ m/s and $\tau_B = 2\pi/N_B = 10$ min.) Figures 2a and 2b show the results for a GW with $\lambda_x = 200$ km and $\tau_{Ir} = 22.5$ min. In Figure 2a, $\lambda_z = -100$ km and $\nu = 0$. Increasing time (for a fixed x) can be seen by decreasing x (for a fixed t). As a fluid particle's vertical velocity increases to its maximum value then decreases to zero at the top of its upward displacement (in time), note that the density perturbation is maximum (because denser air has been moved up),

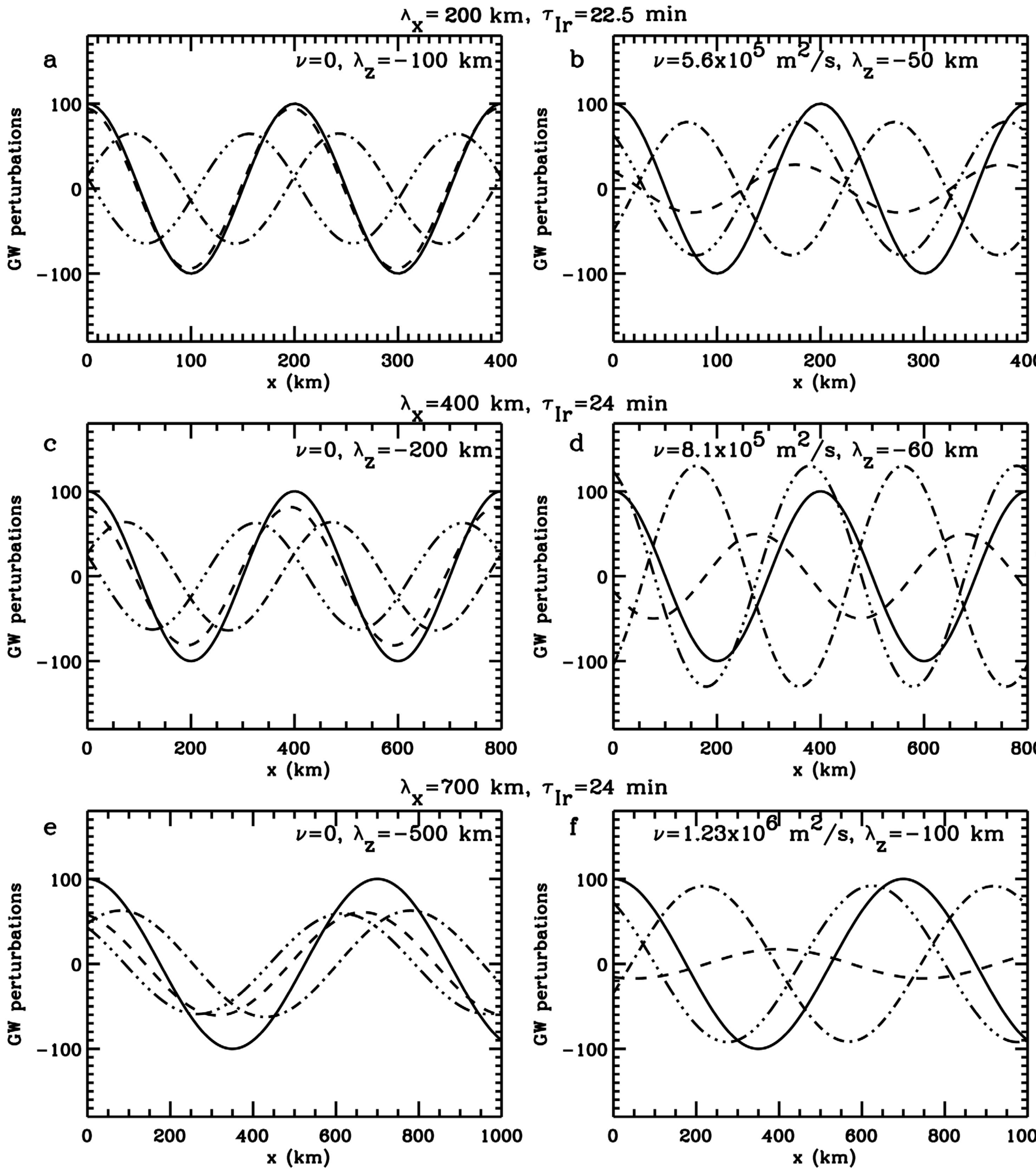

Fully compressible, dissipative polarization relations

Figure 2. $\widetilde{u}$ (solid), $2\widetilde{w}$ (dash), $500\widetilde{T}/\overline{T}$ (dash-dot), and $500\widetilde{\rho}/\overline{\rho}$ (dash-dot-dot-dot) for an eastward propagating GW. Row 1: $\lambda_x = 200$ km and $\tau_{Ir} = 22.5$ min. (a) $\lambda_z = -100$ km and $\nu = 0$. (b) $\lambda_z = -50$ km and $\nu = 5.6 \times 10^5$ m^2/s. Row 2: $\lambda_x = 400$ km and $\tau_{Ir} = 24$ min. (c) $\lambda_z = -200$ km and $\nu = 0$. (d) $\lambda_z = -60$ km and $\nu = 8.1 \times 10^5$ m^2/s, respectively. Row 3: $\lambda_x = 700$ km and $\tau_{Ir} = 24$ min. (e) $\lambda_z = -500$ km and $\nu = 0$. (f) $\lambda_z = -100$ km and $\nu = 1.23 \times 10^6$ m^2/s, respectively. $\widetilde{u}_0$ is set to 100 m/s in each panel. The values of ν were chosen large enough in b,d,f so that significant phase shifts could be seen.

and the temperature perturbation is minimum (because of adiabatic cooling). Figure 2b shows how the phases and amplitudes change after the GW has strongly dissipated. As shown in VF05 and described physically in section 2.3, $|\lambda_z|$ decreases as a GW within a wave packet (from a spatially and temporally localized source) dissipates in an isothermal atmosphere. For $\nu = 5.6 \times 10^5$ m^2/s, the corresponding vertical wavelength is $\lambda_z = -50$ km. Here we have kept τ_r fixed because τ_r only changes if the time derivative of the background wind is non-zero [*Eckermann and Marks*, 1996]. The decrease in $|\lambda_z|$ can be seen most easily from the anelastic GW dispersion relation. For Pr = 1 and $c_s^2 \rightarrow \infty$, equation (12) becomes

$$\left(\omega_{Ir} + \frac{m\nu}{\mathcal{H}}\right)^2 = \frac{k_H{}^2 N_B{}^2}{k_H{}^2 + m^2 + 1/4\mathcal{H}^2} \tag{23}$$

(equation (58) of VF05).For an upward-propagating GW, $m < 0$. As mentioned above, $real(\omega_r)$ is constant along a raypath. Therefore, as ν increases exponentially with z, the left-hand-side of equation (23) decreases in z. This decrease is compensated for by an increase in m^2 on the right-hand-side of equation (23). Therefore, as an upward-propagating GW in a wave packet from a temporally and spatially localized source dissipates in an isothermal atmosphere, $|\lambda_z|$ decreases.

[25] Figure 2b shows the solution. While $\tilde{u}$ and $\tilde{w}$ are in phase for this GW when $\nu = 0$, $\tilde{w}$ lags $\tilde{u}$ after the GW has dissipated. Additionally, strong dissipation causes $\tilde{u}$ and $\tilde{\rho}$ to be nearly in phase, and for $\tilde{T}$ to lead $\tilde{u}$ by more than 90°. Note that $\tilde{\rho}$ and $\tilde{T}$ are 180° out of phase after the GW has dissipated. Additionally, $\tilde{w}_0/\tilde{u}_0$ decreased, while $\tilde{T}_0/\tilde{u}_0$ and $\tilde{\rho}_0/\tilde{u}_0$ increased after strong dissipation. (As we show in a moment, until the GW strongly dissipates, $\tilde{w}_0/\tilde{u}_0$ increases in z if $\overline{T}$ increases.) Figures 2c and 2d show the corresponding results for a GW with λ_x = 400 km and τ_{Ir} = 24 min. In Figure 2c, $\lambda_z = -200$ km and $\nu = 0$, and in Figure 2d, $\lambda_z = -60$ km and $\nu = 8.1 \times 10^5$ m^2/s. Before the GW dissipates (c), compressible effects are important; e.g., the phase shift between $\tilde{T}$ and $\tilde{\rho}$ is significantly less than 180°. After the GW strongly dissipates (d), $\tilde{w}_0/\tilde{u}_0$ has decreased, and $\tilde{T}_0/\tilde{u}_0$ and $\tilde{\rho}_0/\tilde{u}_0$ have increased.

[26] Figures 2e and 2f show the results for a GW with λ_x = 700 km and τ_{Ir} = 24 min. In Figure 2e, $\lambda_z = -500$ km and ν = 0, and in Figure 2f, $\lambda_z = -100$ km and $\nu = 1.23 \times 10^6$ m^2/s. As before, compressible effects are clearly important prior to dissipation, causing the phases of all components to be within 30° of each other. After strong dissipation, the phase difference between $\tilde{\rho}$ and $\tilde{T}$ has increased significantly, while $\tilde{w}$ now lags behind $\tilde{u}$ significantly (by ~80°). Additionally, $\tilde{w}_0/\tilde{u}_0$ has decreased significantly after strong dissipation. Thus, Figure 2 demonstrates that the phases and amplitude ratios of a GW changes after it undergoes strong dissipation.

[27] Finally, we note that the phase shifts and amplitude ratios during strong dissipation are significantly different when Pr = 1 (not shown).

3.3. Dissipating GWs in Idealized Thermospheres

[28] In this section, we show the phase shifts and amplitude ratios of dissipating medium and large-scale GWs as a function of altitude. We then calculate these values as a function of $\overline{T}$ and ν for a large range of GWs. Because we wish to have generic results which do not depend on the background wind, we set $\overline{U} = \overline{V} = 0$. We also choose simple temperature profiles which only vary in z. Figure 3 shows the background temperature, mean density, density scale height $\mathcal{H}$, kinematic viscosity, mean molecular weight X_{MW}, γ, buoyancy frequency N_B, and sound speed c_s profiles. The exospheric temperatures range from extreme solar minimum ($\overline{T} = 600$ K) to extreme solar maximum ($\overline{T} = 1500$ K). The analytic functions for $\overline{T}$, X_{MW} and γ are given in *Vadas* [2007]. The decrease of X_{MW} and increase of γ with altitude represent the change in composition from primarily diatomic N_2 and O_2 to monotomic O. The coefficient of molecular viscosity is $\mu = 3.34 \times 10^{-4}\overline{T}^{0.71}$ gm/m/s [*Dalgarno and Smith*, 1962]. The buoyancy period is $\tau_B = 2\pi/N_B$.

[29] First, we ray trace high-frequency, eastward-propagating GWs from $z = 0$ into the thermosphere with an exospheric temperature of $\overline{T} = 1000$ K (dotted lines in Figure 3). We utilize the ray trace model described in VF05, *Vadas* [2007] and *Vadas and Fritts* [2009]. Rows 1–4 of Figure 4 show GWs with λ_x = 40, 200, 400 and 700 km, respectively. At $z = 0$, these GWs have $\lambda_z = -10, -50, -100$ and -200 km, respectively. In Figures 4a, 4d, 4g, and 4j, the solid lines show $-\lambda_z$, and the dotted lines show the horizontal fluxes of vertical momentum (normalized arbitrarily to fit into each plot). As a GW propagates in the thermosphere, λ_z changes in response to $\overline{T}$. Where N_B increases rapidly in the upper mesosphere at $z \sim 80$ km, $|\lambda_z|$ decreases. This decrease is especially significant for large $|\lambda_x|$. Where N_B decreases at $z \geq 120$ km, $|\lambda_z|$ increases [*Vadas and Fritts*, 2006]. This increase is especially significant for large $|\lambda_x|$. The GWs in rows 1–4 have maximum momentum fluxes (i.e., $z_{\rm diss}$) at $z \sim 125$, 220, 250 and 260 km, respectively. Above these altitudes, dissipation is strong. Because the GW in row 1 dissipates where $\overline{T}$ is still increasing, $|\lambda_z|$ continues to increase approximately linearly with altitude even during strong dissipation. However, $|\lambda_z|$ decreases at and above the dissipation altitudes for the GWs in rows 2–4, because $\overline{T}$ is approximately constant at those altitudes (VF05). Therefore, whether or not $|\lambda_z|$ increases or decreases above $z_{\rm diss}$ depends on $\overline{T}$ and λ_x.

[30] Note that the WKB ray trace solutions shown in Figure 4 may only be valid $\sim\mathcal{H}$ above the dissipation altitude, because the residues can become larger than one there [*Vadas*, 2007]. This is because strong dissipation may cause a GW to partially reflect downward as it continues to propagate upwards [*Midgley and Liemohn*, 1966; *Yanowitch*, 1967; *Volland*, 1969b; *Maeda*, 1985]. When this occurs, a GW can no longer be represented by a single upgoing or downgoing wave, causing ray theory to break down if the reflected wave amplitude is significant. This effect is not important for GWs with $|\lambda_z| \ll 4\pi\mathcal{H}$, but can become important for GWs with very large vertical wavelengths of $|\lambda_z| > 4\pi\mathcal{H}$ [*Yanowitch*, 1967].

[31] Figures 4b, 4e, 4h, and 4k show the velocity perturbations, and Figures 4c, 4f, 4i, and 4l show the temperature and density perturbations, of the GWs as they propagate and dissipate. Because the GW in row 1 has $|\lambda_z| \ll 4\pi\mathcal{H}$, it follows the Boussinesq phase relations prior to dissipating (e.g., $\tilde{u}$ and $\tilde{w}$ are in phase, while $\tilde{T}$ and $\tilde{\rho}$ are 180° out-of-phase). This appears to be the case also for $z > z_{\rm diss}$ while the GW amplitude is non-negligible. However, for the GWs in rows 2–4, the phase shift between $\tilde{T}$ and $\tilde{\rho}$ are much smaller than 180° well below the dissipation altitude because of compressible effects that are important when $|\lambda_z| > 2\pi\mathcal{H}$. As $\mathcal{H}$ increases and $|\lambda_z|/(2\pi\mathcal{H})$ decreases, however, and as these GWs dissipate, the phase shift between $\tilde{T}$ and $\tilde{\rho}$ increases substantially. For example, the phase shift

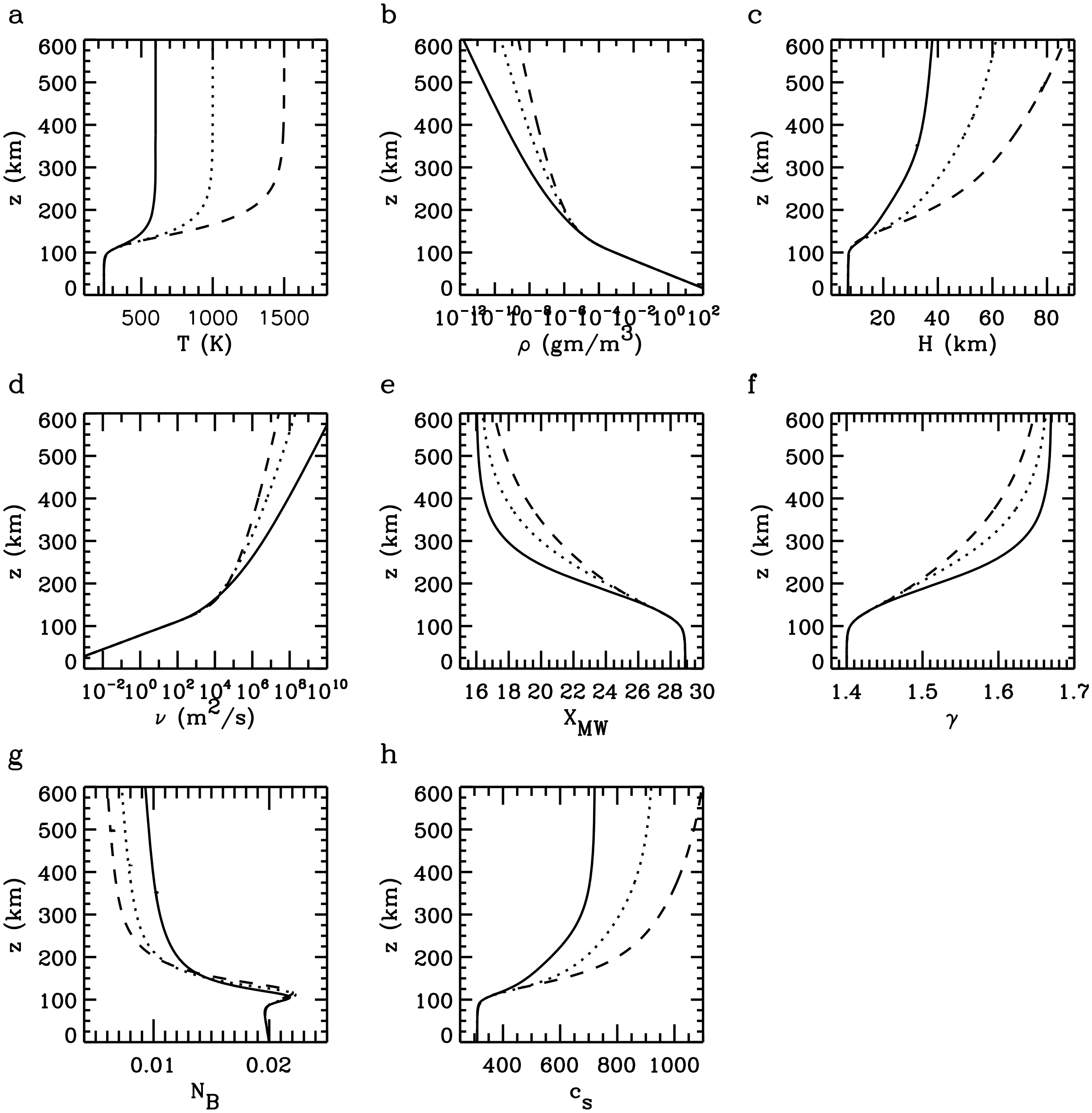

Figure 3. Vertical profiles of the background parameters from 3 idealized temperature profiles with exospheric temperatures of $\overline{T} = 600$ K (solid lines), $\overline{T} = 1000$ K (dotted lines), and $\overline{T} = 1500$ K (dashed lines). (a) Temperature $\overline{T}$. (b) Mean neutral density $\overline{\rho}$. (c) Density scale height $\mathcal{H}$. (d) Kinematic viscosity $\nu = \mu/\overline{\rho}$. (e) Mean molecular weight of a particle in the gas, X_{MW}. (f) γ. (g) Buoyancy frequency N_B (in rad/s). (h) Sound speed c_s (in m/s).

between $\tilde{\rho}$ and $\tilde{T}$ at $z < 100$ km in Figure 4i is $\sim 90°$, and increases to 170° when the GW strongly dissipates (at $z \sim 270$ km). There is a similar (although smaller) shift between $\tilde{u}$ and $\tilde{w}$ over this altitude range.

[32] We also see that $\tilde{w}_0/\tilde{u}_0$ increases significantly from $z \simeq 50$ to 200 km in Figure 4h; this ratio only decreases when the GW strongly dissipates at $z > 280$ km. We now show that this increase occurs because $|\lambda_z|$ increases substantially ($\sim$40%) over this altitude range. Figure 5a shows a close-up of $\tilde{w}$ (dotted line) for the GW in row 3 of Figure 4. The dashed line shows $\tilde{w}$ calculated from equations (15), (12), and (18)–(19) assuming $\nu = 0$, but taking the values of m and $\tilde{u}$ from the dissipative solutions. There is only a small difference between these lines, even when the GW dissipates strongly. Therefore, the increase in $\tilde{w}_0/\tilde{u}_0$ before strong dissipation occurs because $|\lambda_z|$ increases substantially in altitude. This is not surprising, considering the 2D Boussinesq relation is $\tilde{w}_0/\tilde{u}_0 = |\lambda_z/\lambda_x|$. Note that $|\lambda_z|$ increases from $z \simeq 50$ to 200 km because $\overline{T}$ increases there. Figure 4 demonstrates that the phase and amplitude relationships between GW components are sensitive to λ_H, λ_z, $\overline{T}$, $\mathcal{H}$, and N_B.

[33] We now show a result which we mentioned in section 2.3. In Figure 5b, we show the vertical group velocity $c_{gz} \equiv \partial\omega_{Ir}/\partial m$ and the negative of the vertical phase

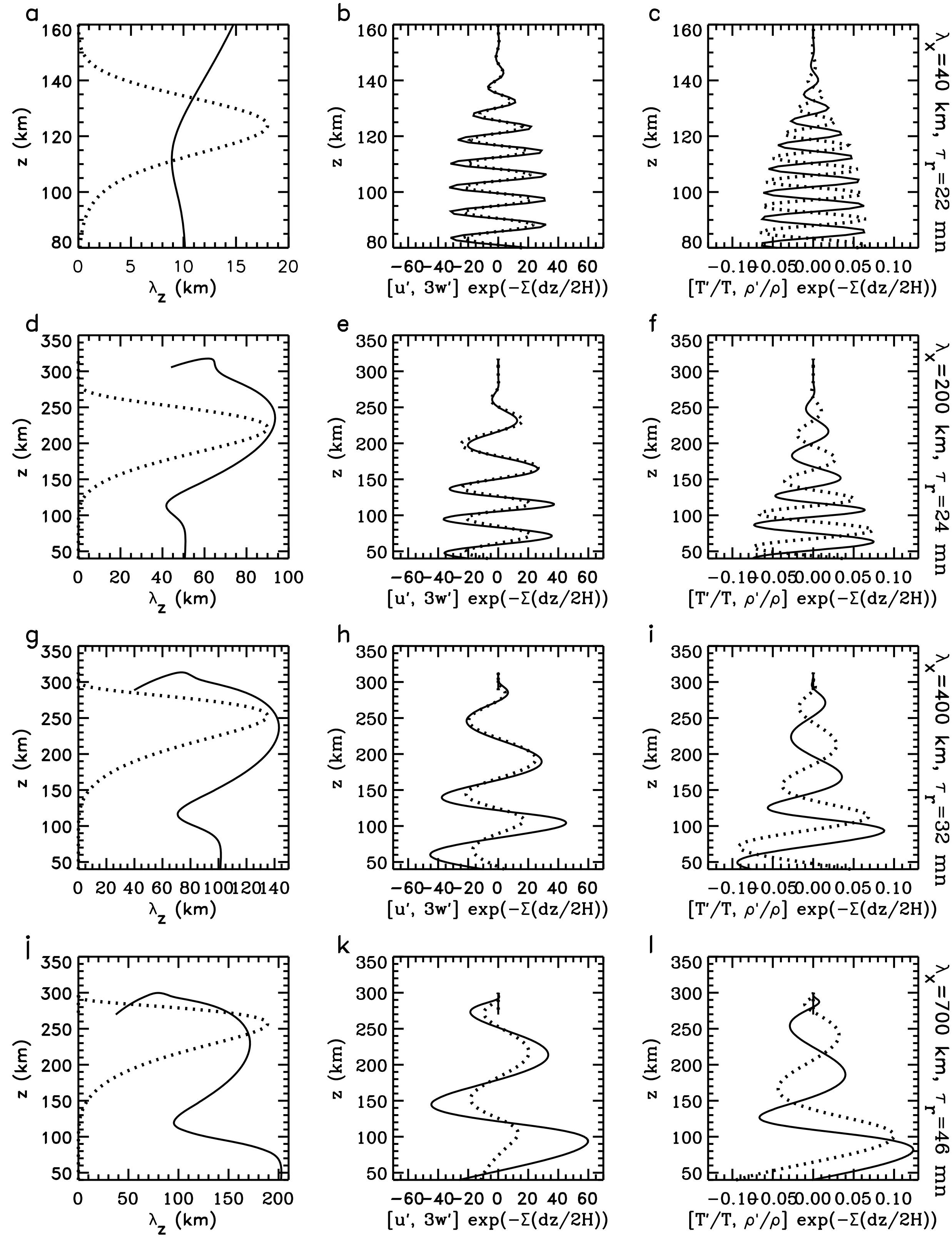

Figure 4. Characteristics of upward and eastward-propagating GWs before and during dissipation in a windless atmosphere using the background parameters shown as dotted lines in Figure 3. Row 1: λ_x = 40 km, τ_r = 22 min. Row 2: λ_x = 200 km, τ_r = 24 min. Row 3: λ_x = 400 km, τ_r = 32 min. Row 4: λ_x = 700 km, τ_r = 46 min. Figures 4a, 4d, 4g, and 4j show $-\lambda_z$ (solid), $\overline{u'w'}$ (dotted) (arbitrary normalization). Figures 4b, 4e, 4h, and 4k show $\widetilde{u}\exp(-\Sigma dz/2\mathcal{H})$ (solid), $3\widetilde{w}\exp(-\Sigma dz/2\mathcal{H})$ (dotted). Figures 4c, 4f, 4i, and 4l show $(\widetilde{T}/\overline{T})\exp(-\Sigma dz/2\mathcal{H})$ (solid), $(\widetilde{\rho}/\overline{\rho})\exp(-\Sigma dz/2\mathcal{H})$ (dotted). Note that the y-axis scale is different in row 1.

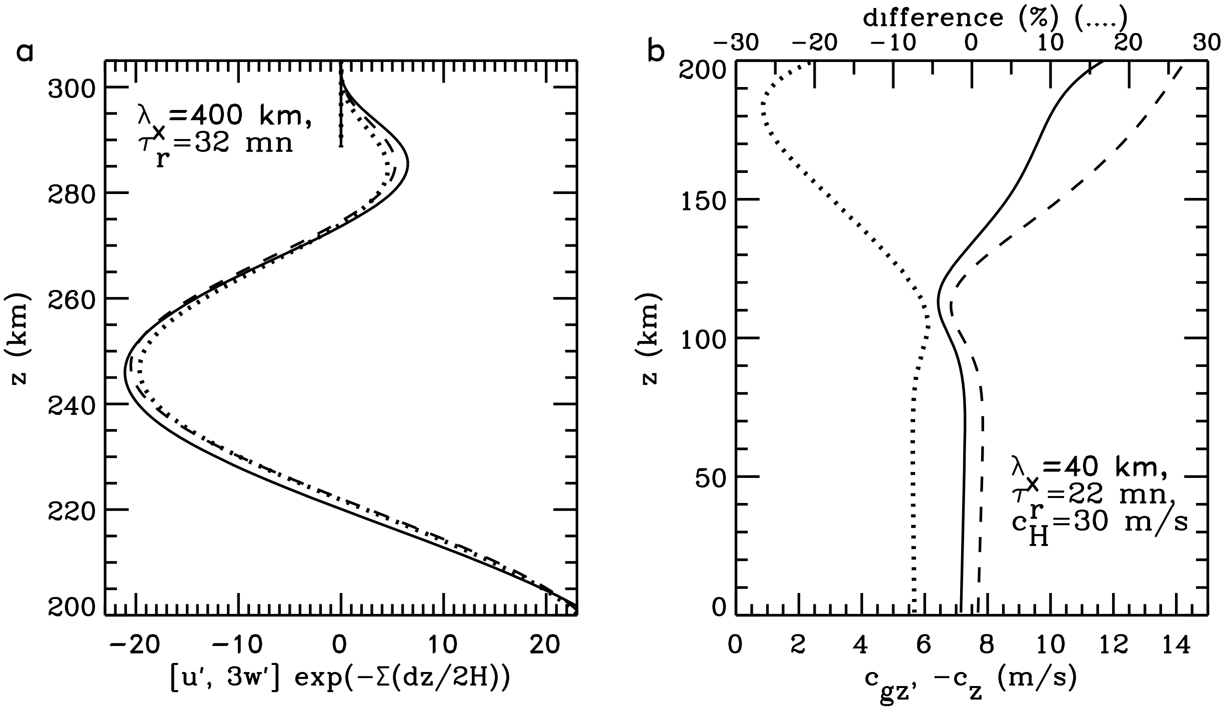

Figure 5. (a) Close-up for the GW in row 3 of Figure 4. $\widetilde{u}\exp(-\Sigma dz/2\mathcal{H})$ (solid) and $3\widetilde{w}\exp(-\Sigma dz/2\mathcal{H})$ (dotted) from ray tracing. The dashed line shows $\widetilde{w}$ calculated from equations (15), (12), and (18)–(19) assuming $\nu = 0$. (b) c_{gz} (solid) and $-c_z = -\omega_{Ir}/m$ (dashed) for the GW in row 1 of Figure 4. The difference (in percent) is shown by the dotted line. Note that this GW is different from the one shown in Figure 5a.

speed $-c_z \equiv -\omega_{Ir}/m$ for a GW similar to that shown in *Walterscheid and Hickey* [2011]. Here, we use the GW in row 1 of Figure 4. (Thus, this is a different GW than displayed in Figure 5a.)

[34] We see that these velocities are within 8% up to $z_{\text{diss}} \sim 120$ km. At altitudes below z_{diss}, the most significant difference between c_{gz} and $-c_z$ occurs in the lower atmosphere where dissipation is completely negligible ($\nu \simeq 0$). This large difference occurs there because the vertical group velocity c_{gz} (not the vertical phase velocity c_z) describes the vertical velocity with which the energy in a wave packet propagates [*Lighthill*, 1978]. Above z_{diss}, this difference increases. At $z \sim 155$ km, where the momentum flux is negligible, the difference between c_{gz} and $-c_z$ is still less than 20%. Therefore, when plotting c_{gz} and $-c_z$ from the same wave packet solution, we find these velocities to be reasonably similar. We note, however, that the similarity between c_{gz} and $-c_z$ occurs because $|\lambda_z| \ll 4\pi\mathcal{H}$ for this GW. For GWs with larger $|\lambda_z|$, c_{gz} is quite different from $-c_z$, including in the lower atmosphere where dissipation is insignificant. This is because $-c_z$ is not a good proxy for the vertical speed at which the energy within a wave packet propagates.

[35] For each of the temperature profiles shown in Figure 3, we now visually relate the kinematic viscosity of the fluid with the idealized "observation" altitude, $\mathcal{H}$, N_B, and c_s. We do this in order to "look back" and determine the altitudes at which succeeding plots refer to. Figure 6 can also be used to estimate ν, $\mathcal{H}$, N_B, and c_s if the measurement altitude and approximate exospheric temperature are known. We draw invisible vertical lines in Figure 3d for $\nu = 10^2$, 10^3, 10^4, 10^5, 10^6, 10^7, and 10^8 m^2/s. The corresponding altitudes (where these lines intersect the solid, dotted, and dash lines in Figure 3d) are shown in Figure 6a as triangles. The exospheric temperature of each temperature profile is shown on the x-axis. Here, the exospheric temperature is the value of $\overline{T}(z)$ as $z \to \infty$. For example, $\nu = 10^6$ m^2/s occurs at the altitudes of $z \sim 260$, 300, and 350 km for the solid, dotted, and dashed temperature profiles shown in Figure 3a, respectively. Figures 6b–6d show $\mathcal{H}$, N_B, and c_s as a function of the exospheric temperature for the same values of ν.

[36] Figure 7 shows the phase shifts between $\widetilde{u_H}$, $\tilde{w}$, $\tilde{\rho}$, and $\tilde{T}$ for upward propagating GWs during extreme solar minimum (solid lines in Figure 3). Shown are GWs with horizontal wavelengths of $\lambda_H = 20$ to 2000 km and $-\lambda_z = 10$ to 800 km. Remember that $\lambda_z < 0$ for upward-propagating GWs. Rows 1–5 show $\nu = 0$, 10^3, 10^4, 10^5, and 10^6 m^2/s, respectively. Figure 8 shows the corresponding amplitude ratios, $\widetilde{w}_0/\widetilde{u_{H0}}$, $(100\widetilde{\rho}_0/\overline{\rho})/\widetilde{u_{H0}}$, and $\left(100\widetilde{T}_0/\overline{T}\right)/\widetilde{u_{H0}}$, where the velocities are in m/s. From equation (17) of *Vadas and Crowley* [2010], a GW dissipates rapidly above the altitude given by

$$\epsilon \simeq \frac{|k_H m| N_B}{\mathcal{H}\left(\mathbf{k}^2 + 1/4\mathcal{H}^2\right)^{3/2} |\mathbf{k}^2 - 1/4\mathcal{H}^2| \left(1 + \mathrm{Pr}^{-1}\right)\nu}. \quad (24)$$

Here, $\epsilon \simeq 1$ when a GW's momentum flux is maximum (i.e., at $z = z_{\text{diss}}$), $\epsilon \gg 1$ when a wave is not yet dissipating, and $\epsilon \ll 1$ when a wave is strongly dissipating. Since we only wish to display those GWs which have not yet strongly

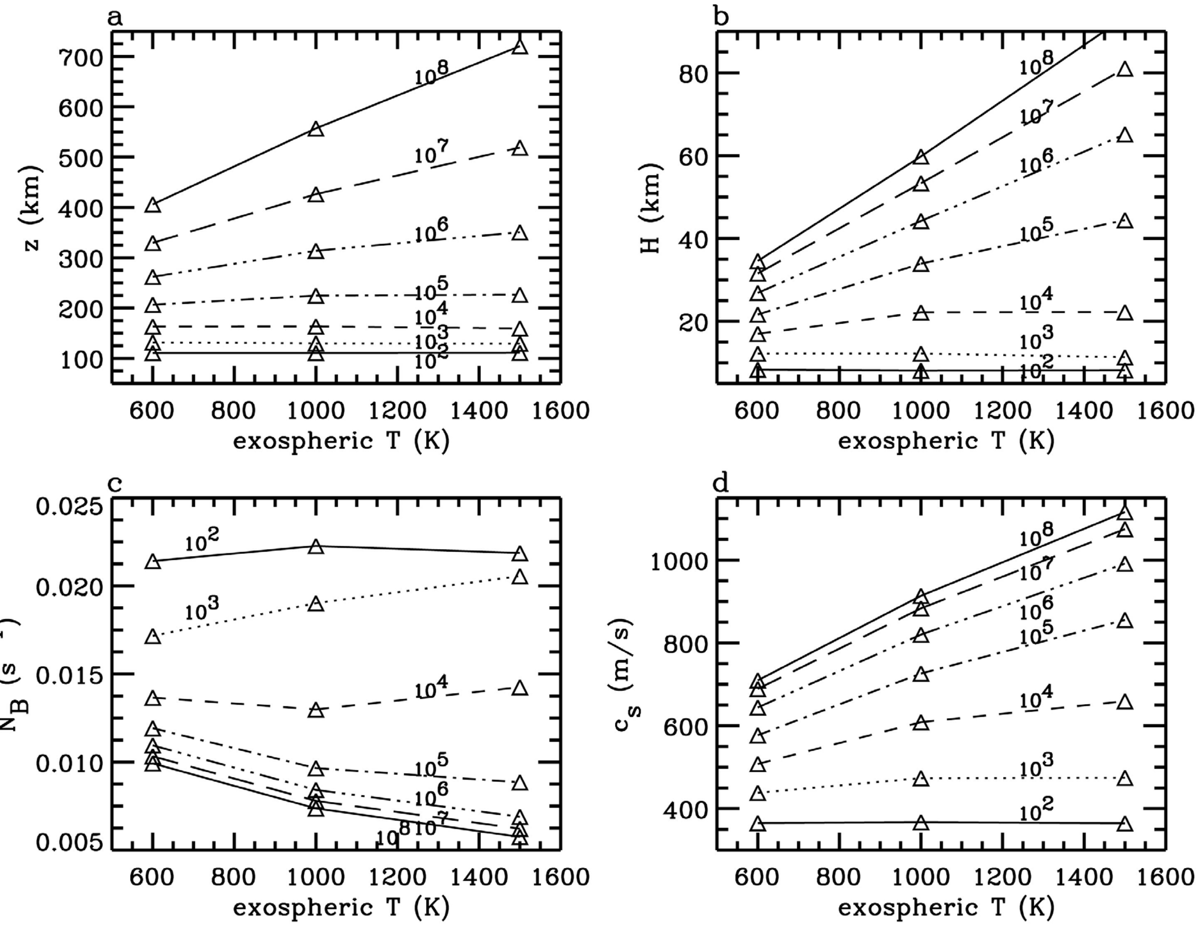

Figure 6. (a) The altitude z where $\nu = 10^2$, 10^3, 10^4, 10^5, 10^6, 10^7, and 10^8 m^2/s for the 3 temperature profiles shown in Figure 3a (triangles). The exospheric temperature of each profile is shown on the x-axis. (b–d) The density scale height $\mathcal{H}$, buoyancy frequency N_B, and sound speed c_s for the same ν values from Figure 6a (triangles). Solid, dotted, short dashed, dashed-dotted, dash-dot-dot-dotted, long dash, and solid lines show $\nu = 10^2$, 10^3, 10^4, 10^5, 10^6, 10^7, and 10^8 m^2/s, as labeled.

dissipated, we hatch out those GWs with $\epsilon < 0.1$. We also hatch out those GWs where a reasonable GW frequency (i.e., $0 < \omega_{Ir} < N_B$) was not found.

[37] For GWs with small $|\lambda_z| < 20$ km (which satisfy the Boussinesq approximation), $\widetilde{w}$ and $\widetilde{u}$ are approximately in phase, $\widetilde{\rho}$ lags $\widetilde{u}$ by 90°, and $\widetilde{T}$ leads $\widetilde{u}$ by 90°. $\widetilde{T}$ and $\widetilde{\rho}$ are 180° out of phase because the pressure perturbations are negligible; the ideal gas law is then $\rho T \simeq constant$, which yields $\widetilde{\rho} \simeq -\widetilde{T}$. The Boussinesq mass continuity equation is $\nabla.\mathbf{v} \simeq 0$ [*Kundu*, 1990]; this implies $\widetilde{w}_0/\widetilde{u_H}_0 \simeq -\lambda_z/\lambda_H$. This result is seen in Figure 8a for small $|\lambda_z| \ll 2\pi\mathcal{H}$. For these GWs, the density perturbations are small, being only $100\widetilde{\rho}_0/\overline{\rho} \sim (0.15\ \mathrm{s/m})\widetilde{u_H}_0$ (i.e., a 7 m/s horizontal velocity perturbation is associated with a 1% density perturbation).

[38] As $|\lambda_z|$ increases and compressible effects become important, the density perturbation amplitudes for very high frequency GWs (with $\omega_{Ir} \simeq N_B$) increases to $100\widetilde{\rho}_0/\overline{\rho} \sim (1.0\ \mathrm{s/m})\widetilde{u_H}_0$ for $\lambda_H < 40$ km and $|\lambda_z| > 100$ km. This also corresponds to a larger phase shift between $\widetilde{\rho}$ and $\widetilde{u_H}$ of $-120°$. For large $|\lambda_z|$ and $\lambda_H \gg 100$ km, the phase shift between $\widetilde{\rho}$ and $\widetilde{u_H}$ decreases to $-10°$, the phase shift between $\widetilde{w}$ and $\widetilde{u_H}$ increases to $-70°$, and the phase shift between $\widetilde{T}$ and $\widetilde{u_H}$ decreases to 10°. For large $|\lambda_z|$, the phase shift between $\widetilde{\rho}$ and $\widetilde{T}$ decreases significantly for $\lambda_H > |\lambda_z|$, and decreases only slightly for $\lambda_H \ll |\lambda_z|$.

[39] As ν increases, the highest-frequency GWs "disappear" because they reflect downward at lower altitudes when $\omega_{Ir} \sim N_B$ due to the decrease of N_B in the thermosphere. Additionally, the lowest-frequency GWs with small $|\lambda_z|$ disappear because they dissipate at lower altitudes. For the remaining GWs, the phase shifts and amplitude ratios depend sensitively on λ_H, λ_z, $\mathcal{H}$, $\overline{T}$, N_B, and ν. For example, the phase shift between $\widetilde{\rho}$ and $\widetilde{u_H}$ is $-45°$ and $-70°$ for GWs with $(\lambda_H, \lambda_z) = (200, 100)$ km for $\nu = 0$ and 10^5 m^2/s, respectively. We say GWs, not GW, however, because we have fixed λ_z in these examples, whereas $|\lambda_z|$ increases or decreases in z for a single GW, as discussed previously.

[40] Figures 9 and 10 show the phase shifts and amplitude ratios for upward-propagating GWs in a thermosphere with an exospheric temperature of 1000 K (dotted lines in Figure 3). Figures 11 and 12 show the corresponding values during solar maximum with an exospheric temperature of 1500 K (dashed lines in Figure 3). Because $\mathcal{H}$ is larger in these figures, compressible effects are less important overall. The phase shifts and amplitude ratios, however, follow

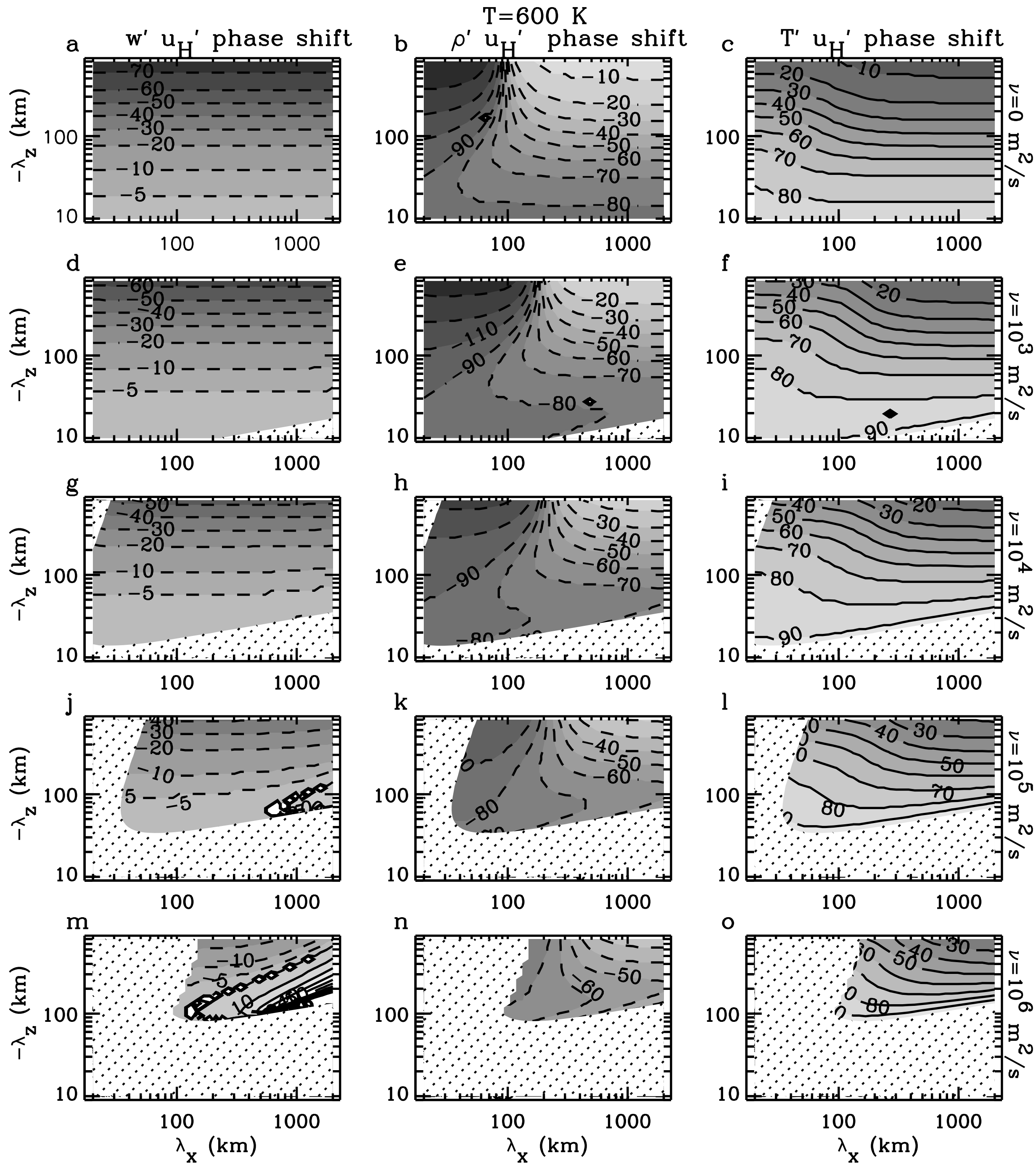

Figure 7. Phase shifts (in degrees) for GWs in a thermosphere with an exospheric temperature of $\overline{T} =$ 600 K. Row 1: $\nu = 0$. (a) Phase shift between $\widetilde{w}$ and $\widetilde{u_H}$. (b) Phase shift between $\widetilde{\rho}$ and $\widetilde{u_H}$. (c) Phase shift between $\widetilde{T}$ and $\widetilde{u_H}$. Rows 2–5: Same as row 1, but for $\nu = 10^3$, 10^4, 10^5, and 10^6 m^2/s, respectively. Solid (dash) lines denote positive (negative) phase shifts (in degrees) in the direction parallel to the GW propagation direction, as labeled. The dotted hatched regions shows $\epsilon < 0.1$ (from equation (24)), or where a reasonable solution (i.e., $0 < \omega_{Ir} < N_B$) was not found.

similar trends as during solar minimum, although with different values.

[41] Suppose a GW is detected in the thermosphere and only some of its properties are measured (e.g., ω_{Ir}, w', and T'). Because the direction of propagation and λ_z are not known, we cannot reverse ray trace this GW in order to determine its source. However, if the background temperature, density scale height, wind, and buoyancy frequency can be measured or inferred from thermospheric models, then Figures 7–12 can be utilized to infer a range of likely λ_H and λ_z. We give examples of how this is done in section 4 and in a companion paper. This method might eventually

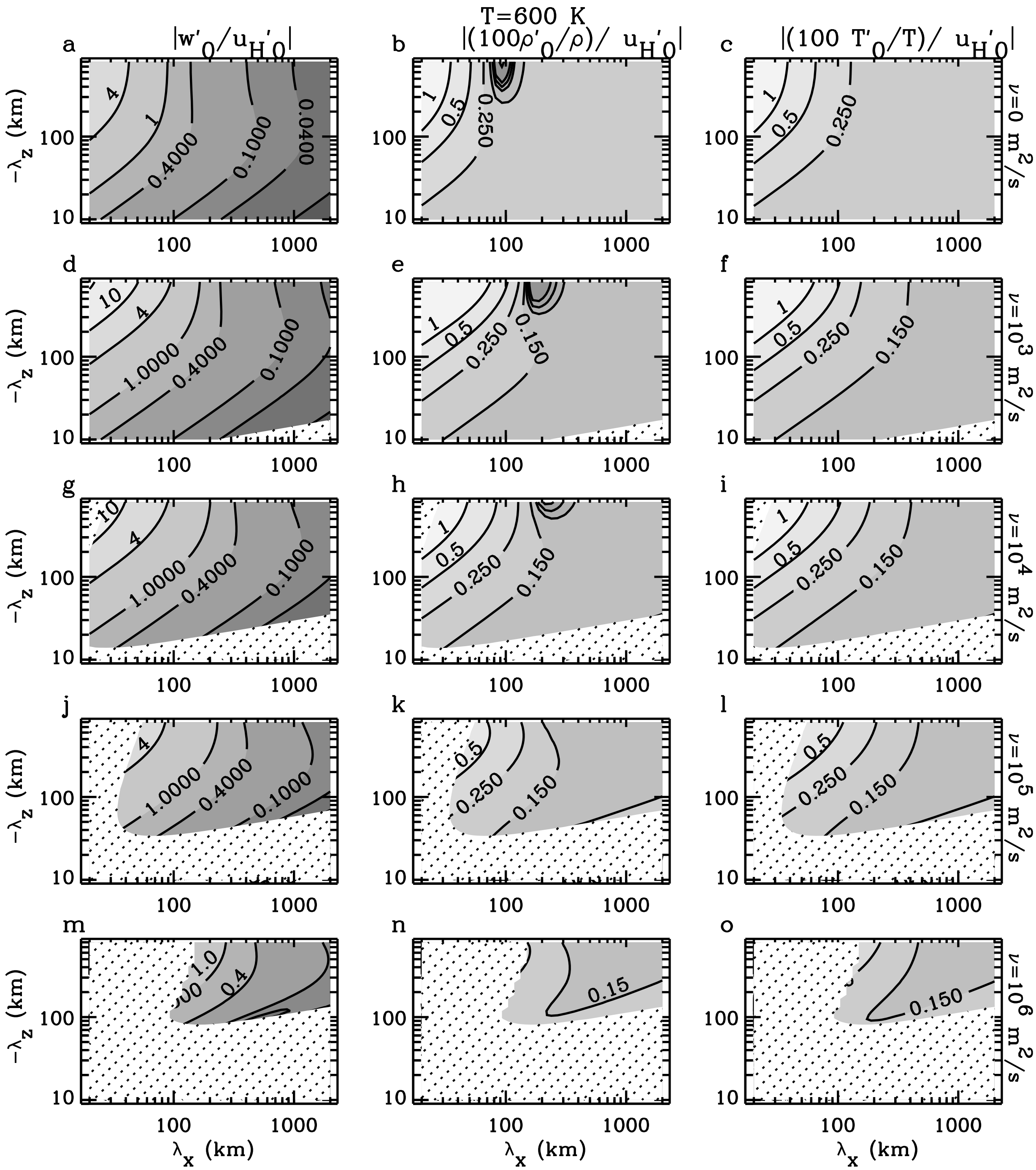

Figure 8. Ratios of GW amplitudes for a thermosphere with an exospheric temperature of $\overline{T} = 600$ K (solid lines). Row 1: $\nu = 0$. (a) $\widetilde{w}_0/\widetilde{u_{H0}}$. (b) $(100\widetilde{\rho}_0/\overline{\rho})/\widetilde{u_{H0}}$. (c) $\left(100\widetilde{T}_0/\overline{T}\right)/\widetilde{u_{H0}}$. $\widetilde{u_{H0}}$ and $\widetilde{w}_0$ are in m/s. Rows 2–5: Same as row 1, but for $\nu = 10^3$, 10^4, 10^5, and 10^6 m^2/s, respectively. The dotted hatched regions are the same as in Figure 7.

lead to a better understanding of the sources of GWs in the thermosphere.

4. Determination of λ_H, λ_z, and ω_{Ir} From In-Situ Satellite Observations

[42] As a satellite orbits the Earth high in the thermosphere, it cuts across the phase lines of propagating GWs. Unfortunately, it most-often cuts across obliquely, rather than perpendicular, to these phase lines. Figure 13 shows a sketch of the satellite path and GW phase lines. If the distance between a perturbation's maximum (or minimum), λ_{track}, is interpreted as a GW's "horizontal" wavelength, then λ_H is (potentially severely) overestimated. Additionally, in-situ satellite measurements cannot measure λ_z (unless limb scans are available), nor can they determine ω_{Ir}. Yet, the sources of these GWs cannot be determined if these

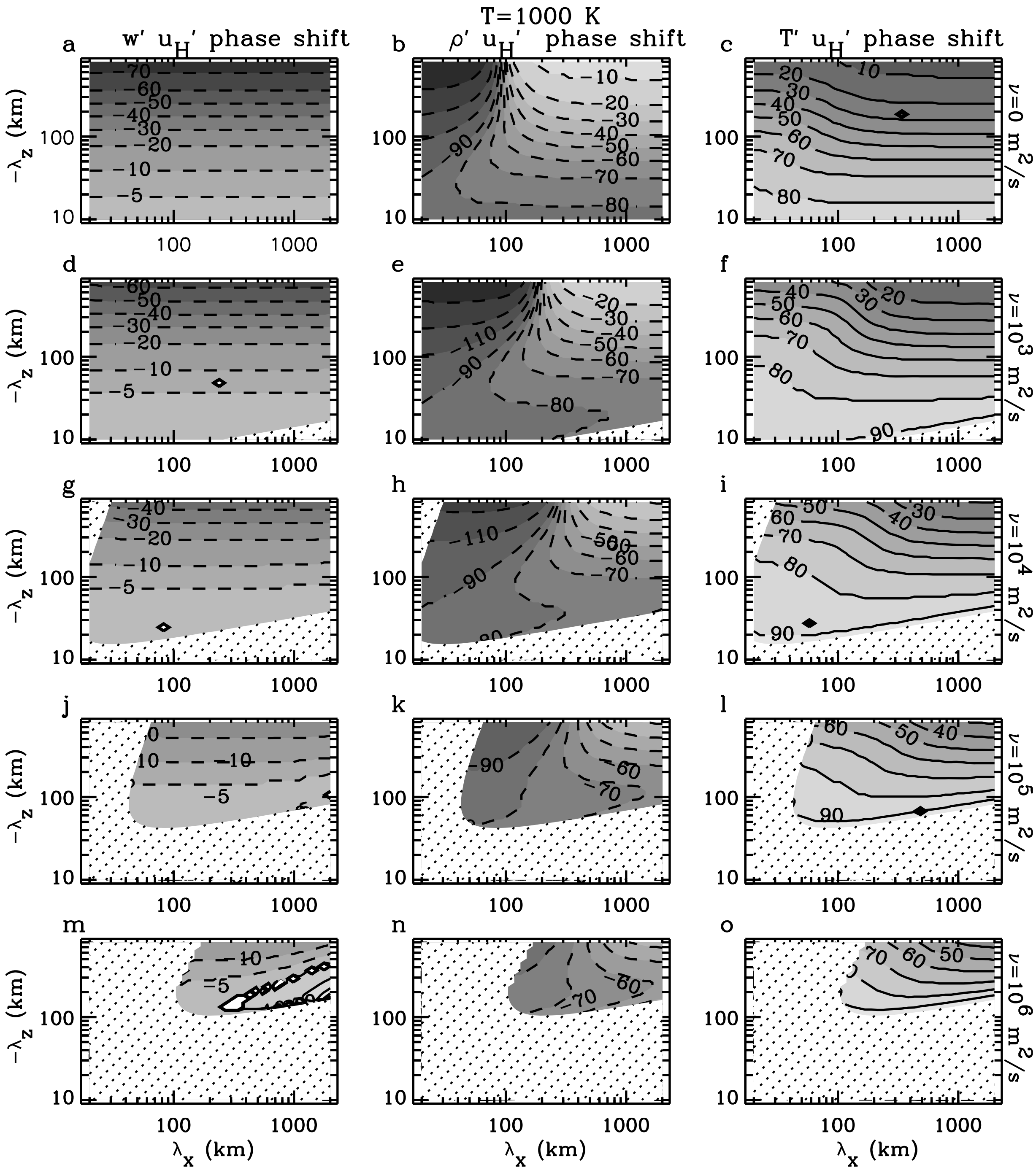

Figure 9. Same as Figure 7 but for an exospheric temperature of $\overline{T} = 1000$ K.

parameters are unknown. Therefore, a reliable method to extract a GW's propagation direction, horizontal and vertical wavelengths, and intrinsic period from in-situ satellite observations would be useful for thermospheric GW studies. The GW dissipative polarization and dispersion relations derived in this paper provide the basis for such a method for medium to large-scale, high-frequency GWs from spatially and temporally variable sources. In this section, we show how λ_H, λ_z, ω_{Ir}, and the propagation direction ψ can be inferred using these relations from in-situ satellite observations of (1) the 3D neutral wind or (2) the vertical velocity, density, temperature and cross-track wind.

[43] For the former case, measured density and/or temperature perturbations can be used to further constrain the inferred GW parameters. It is important to keep in mind the possible sensitivity of the results to the background parameters (i.e., ν, $\overline{T}$, N_B, and $\mathcal{H}$).

4.1. In-Situ Satellite Measurements of the 3D Neutral Wind

[44] Until recently, only the cross-track neutral winds were measured by satellites (e.g., DE2, CHAMP) [*Mayr et al.*, 1990; *Liu et al.*, 2006]. However, recently developed

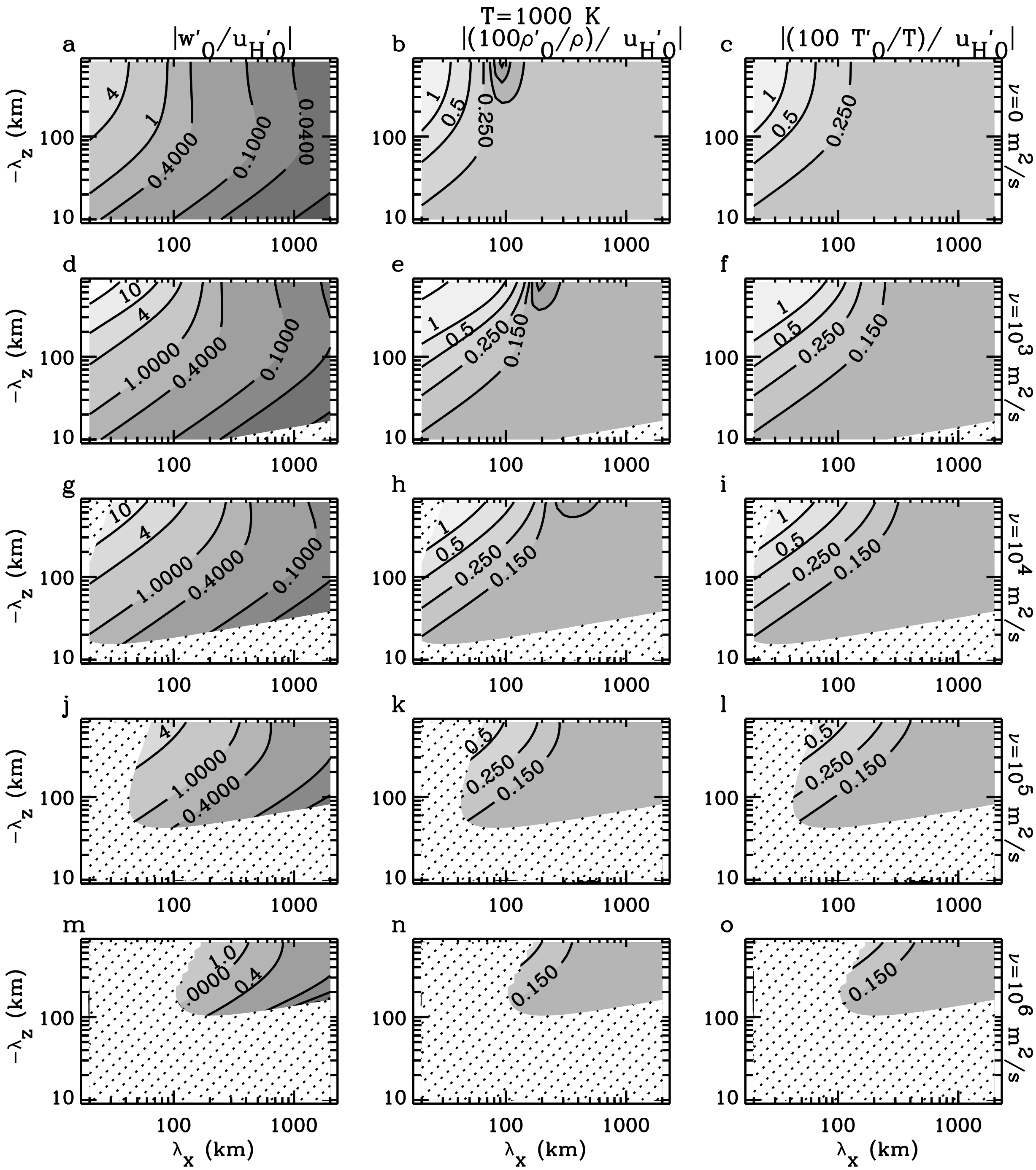

Figure 10. Same as Figure 8 but for an exospheric temperature of $\overline{T} = 1000$ K.

instrumentation may soon allow the three-dimensional wind vector to be determined from orbital platforms. These techniques are described by *Hanson et al.* [1992] and *Earle et al.* [2007]. The first flight of these instruments is part of the CINDI-C/NOFS experiment, for which data analysis is ongoing. We now show how in-situ satellite measurements of the 3D neutral wind can be used to infer λ_H, λ_z, ω_{Ir}, and ψ.

[45] Suppose a satellite is moving at an angle $\theta_{\rm track} = 200°$ north of east, when it observes a wave with velocity perturbations of $u'_0 = 59$ m/s, $v'_0 = 81$ m/s, and $w'_0 = 100$ m/s. Suppose u' and v' are approximately in phase (along the track), and u' (or v') is 176° out of phase with w'. Finally, suppose the distance between wave crests along the satellite track is $\lambda_{\rm track} = 320$ km.

[46] We now obtain the GW's propagation direction in the horizontal plane, ψ. From equation (20), a high-frequency GW propagates in the same direction as its horizontal velocity perturbation u'_H. Using $\tan\psi = v'/u'$, where ψ is the angle north of east, we find $\psi = 54°$ or $\psi = 234°$. Thus, the GW is either propagating northeast or southwestward,

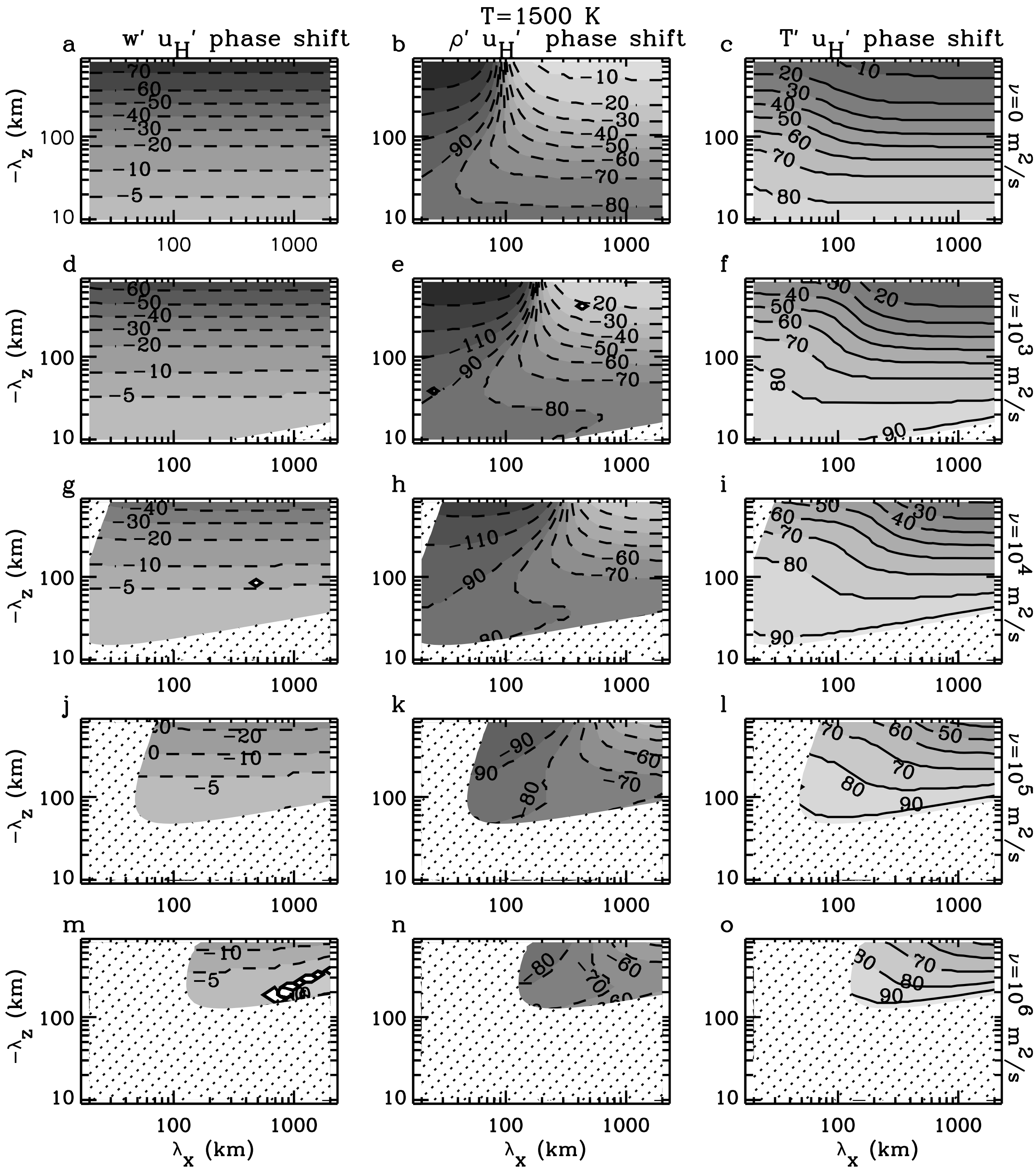

Figure 11. Same as Figure 7 but for an exospheric temperature of $\overline{T}$ = 1500 K.

with a horizontal wind perturbation amplitude of $u'_{H0} = \sqrt{(u'_0)^2 + (v'_0)^2} = 100$ m/s. This ambiguity is determined by the phase shift between u' (or v') and w'. For an upward-propagating GW, u' and w' are "approximately" in phase (out of phase) if the GW is propagating eastward (westward). (By "approximately" in phase, we mean that the absolute value of the phase difference is less than 70° from Figures 7, 9, and 11.) Assuming the wave is upward-propagating, we conclude that this GW must be propagating to the southwest, with an angle ψ = 234°.

[47] It is now easy to determine λ_x and λ_y. If the angle between the satellite track and the wave propagation direction is ϕ, then the wave's horizontal wavelength is related to $\lambda_{\rm track}$ via

$$\lambda_H = \lambda_{\rm track}\cos\phi. \tag{25}$$

Using $\phi = \psi - \theta_{\rm track}$ = 34°, we obtain λ_H = 265 km. The horizontal wave number is $k_H = 2\pi/\lambda_H$. Since $k = k_H\cos\psi$ and $l = k_H\sin\psi$, then $\lambda_x = 2\pi/k = -450$ km and $\lambda_y = 2\pi/l = -330$ km. Thus, λ_H and the horizontal direction of

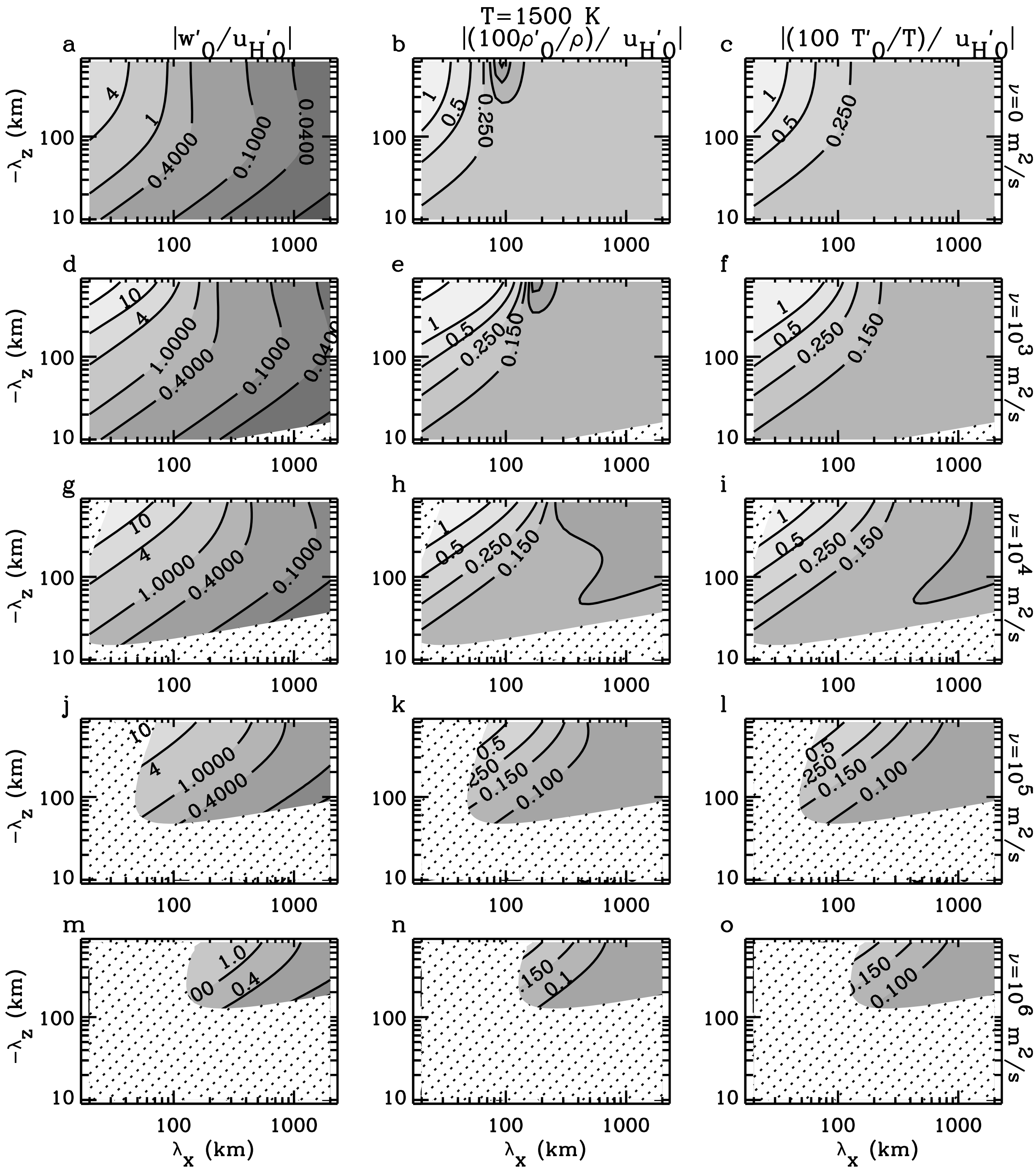

Figure 12. Same as Figure 8 but for an exospheric temperature of $\overline{T} = 1500$ K.

propagation can be easily determined without knowing the background parameters. These background parameters, however, need to be known to determine λ_z and ω_{Ir}.

[48] Suppose the background temperature is $\overline{T} = 1500$ K and the satellite is at an altitude of $z = 350$ km. Using the idealized profiles from Figure 6a, we estimate $\nu \sim 10^6$ m^2/s. Figure 14 shows a blow-up of the solutions for this profile. Since $\lambda_H = 265$ km and $w_0'/u_{H0}' = 1.0$, we deduce a vertical wavelength of $\lambda_z \sim -300$ km and an intrinsic wave period of $\tau_{Ir} \sim 19$ min from Figure 14a. Additionally, Figures 14b and 14c predict that the phase shift between ρ' and u' is $\sim\!-78°$, the phase shift between T' and u' is $\sim\!80°$, $|(100\rho_0'/\overline{\rho})/u_{H0}'| \sim 0.12\ \ (\mathrm{m/s})^{-1}$, and $|(100T_0'/\overline{T})/u_{H0}'| \sim 0.12\ \ (\mathrm{m/s})^{-1}$. These predictions can be tested if the satellite measurements include the neutral density and/or temperatures, thereby further constraining the inferred GW parameters.

4.2. In-Situ Satellite Measurements of the Vertical Velocity, Density, Temperature and Cross-Track Wind

[49] We now show how a GW's λ_H, λ_z, ω_{Ir}, and ψ can be inferred in a simple and straightforward way from in-situ

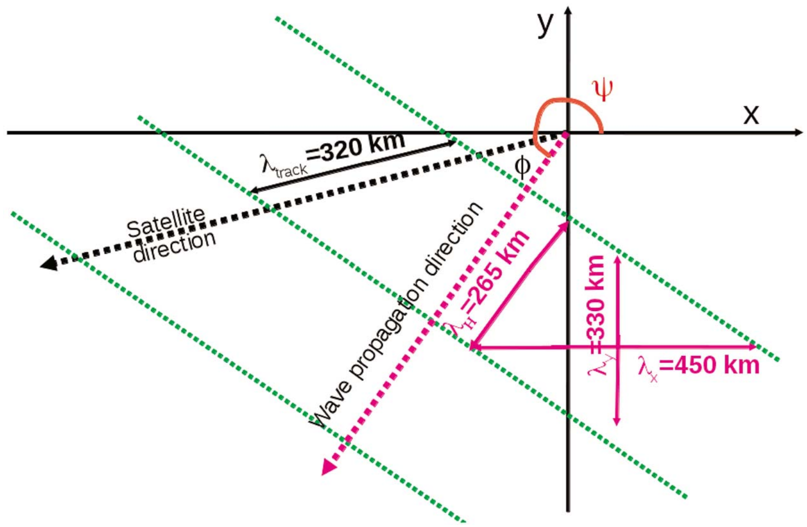

Figure 13. Sketch of a GW encountered by a satellite. Satellite track (short dash black line); GW propagation direction (short dash purple line); GW constant phase lines (dotted green lines). λ_H is the GW horizontal wavelength, and λ_x and λ_y are the zonal and meridional wavelengths. λ_{track} is the apparent horizontal wavelength of the GW as measured by the satellite along its track. ϕ is the angle between the satellite track and wave propagation direction. ψ is the GW propagation angle (north of east).

satellite measurements of w', ρ', T', and the cross-track wind u'_{track}. For this example, we choose a wave observed by the DE2 satellite during orbit 3024 at ~22.1 UT, as reported by *Innis and Conde* [2002]. This wave was observed on 22 February 1982 (during solar maximum) at a high northern latitude (70–90°N). The background neutral temperature increased from $\overline{T} \sim 1100-1400$ K from 22.10 to 22.14 UT. Before 22.08 UT, the satellite was traveling northward at an approximately fixed longitude of 37.4°N. At and after 22.08 UT, the satellite was traveling southward at an approximately fixed longitude of -144.4°N. Since we are only analyzing the published figures (not the data), we do not include error bars here. However, it is straightforward to include them [*Nicolls et al.*, 2012].

[50] Figure 15 shows Figure 1 from IC02. It displays w', $T'/\overline{T}$, and $\rho'/\overline{\rho}$, the fractional oxygen O and N_2 number density perturbations, and u'_{track}, respectively. This figure shows what is assumed to be a "snapshot" of a wave at 22 UT (due to the high speed of the satellite relative to the wave speed.) Note that O is the major species. This, along with the fact that O and N_2 are nearly in phase, causes the plotted density perturbation profile to appear sinusoidal and consist of a single wave. As discussed above, this "single-species" approximation is necessary for use of the theoretical relations derived in this paper. (See *Gross et al.* [1984] for the non-

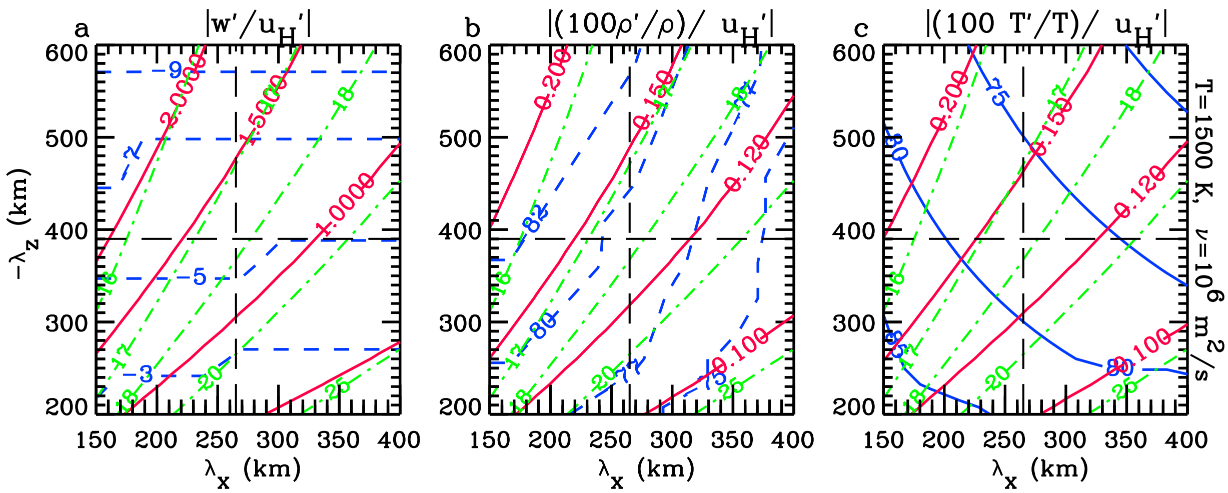

Figure 14. Phase shifts in degrees (blue) and amplitude ratios (red) for a thermosphere with an exospheric temperature of $\overline{T} = 1500$ K (dashed lines in Figure 3) at an altitude such that $\nu = 10^6$ m^2/s. (a) w' with respect to u'_H. (b) $\rho'/\overline{\rho}$ with respect to u'_H. (c) $T'/\overline{T}$ with respect to u'_H. Solid (dash) blue lines denote positive (negative) values. Green dash-dot lines show the intrinsic GW period τ_{Ir} (in minutes).

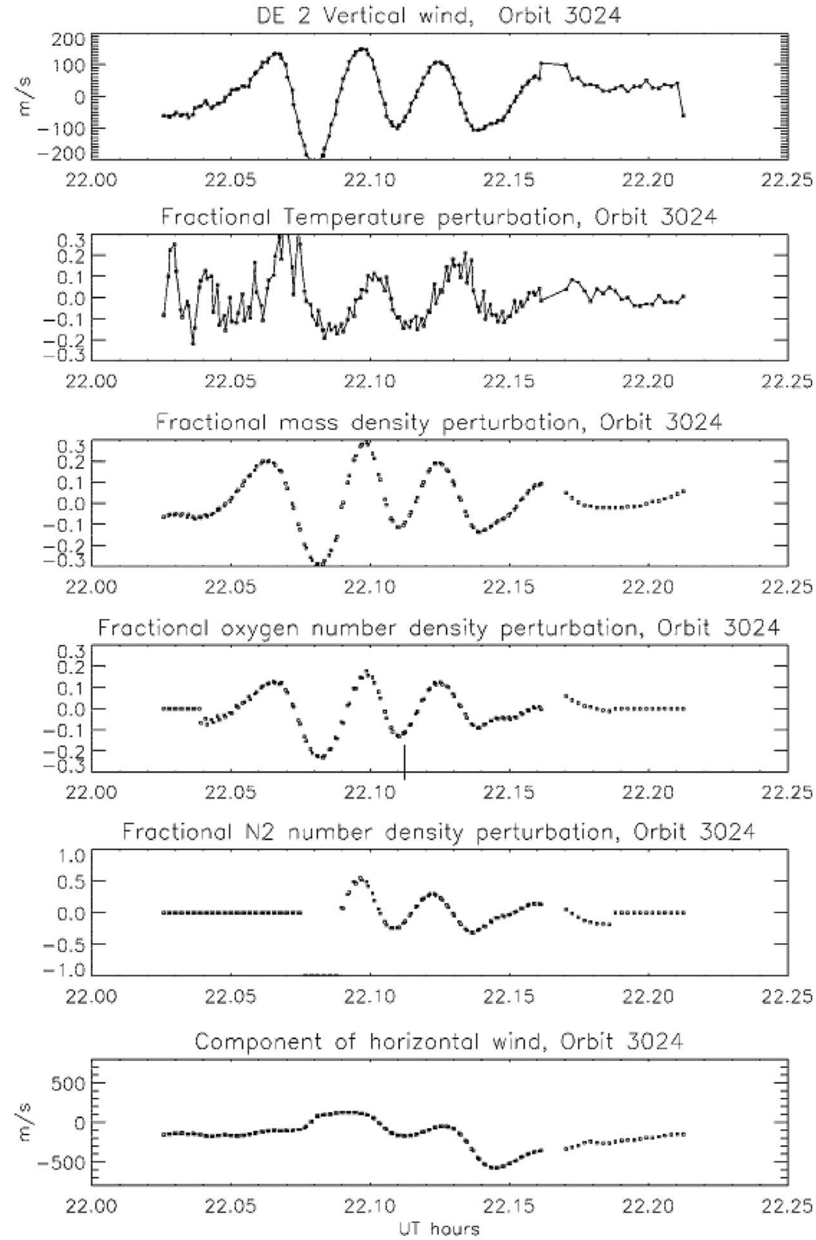

Figure 15. DE2 WATS and NACS data for Orbit 3024, 1982 day 053. Top to bottom: Vertical velocity estimates, fractional neutral temperature perturbation, fractional mass density perturbation, fractional atomic oxygen number density, fractional molecular nitrogen number density, and component of the neutral horizontal wind perpendicular to spacecraft motion.

viscous theory concerning the phase shifts and amplitude ratios of O and N_2 in the thermosphere.) Three wave cycles are seen from 22.05 to 22.15 UT, as the satellite crosses the north pole. At lower latitudes, the wave is not seen, thereby implying that the GW comes from a spatially localized source. (The source may also be temporally localized, although this data cannot show this aspect of the source.) We analyze the GW only from 22.08 to 22.14 UT, when the satellite moves southward. During this time, the satellite's altitude varied from $z \sim 595$ to 535 km. Although there is some variability, the average time between the wave peaks is 105 s. Additionally, w' leads T' (in time) by $\sim$50–110° (along the orbit path), ρ' leads/lags w' by $\sim$−45 to 45°, ρ' leads T' by 40–120°, and u'_{track} lags w' by less than 50°. Finally, $w'_0 \sim 100$–120 m/s, $T'_0/\overline{T} \sim 15\%$, $\rho'_0/\overline{\rho} \sim 15$–$25\%$, and $(T'_0/\overline{T})/(\rho'_0/\overline{\rho}) \sim 0.6$–$1.1$. Thus, $(100\rho'_0/\overline{\rho})/w'_0 \sim 0.1$–$0.25\,(\mathrm{m/s})^{-1}$. Using the satellite velocity of 7.0 km/s, we estimate a distance between the wave crests along the satellite track of $\lambda_{\mathrm{track}} \sim 650$–$800$ km.

[51] We use the DE2 measurements to estimate the background parameters. From 22.08 to 22.14 UT, the average temperature and altitude are $\overline{T} \sim 1200$ K and $z \sim 560$ km, respectively. The DE2 measurements include O, N, He, Ar,

and N_2. According to MSIS E-90 [*Hedin*, 1991], O has the largest number density at this altitude. The next largest are N_2 and He, which have approximately equal number densities. The average mass density is

$$\overline{\rho} = \sum X_i n_i / N_A = \left(28.0N_2 + 16.0O + 4.0He + 40.0Ar + 14.0N\right)/N_A, \tag{26}$$

where X_i is the molecular mass of species i, n_i is the number density of species i, and $N_A = 6.022 \times 10^{23}$ mole^{-1} is Avogadro's number. We estimate $\overline{\rho} \sim 1 \times 10^{-9}$ gm/m^3. The average molecular mass and specific heats are

$$\mathrm{X_{MW}} = \sum X_i n_i / \overline{n} \tag{27}$$

$$C_v = \mathrm{R}\left(\frac{3}{2}(O + He + Ar + N) + \frac{5}{2}(N_2)\right)/\overline{n} \tag{28}$$

$$C_p = \mathrm{R}((1 + 3/2)(O + He + Ar + N) + (1 + 5/2)(N_2))/\overline{n}, \tag{29}$$

respectively, where $\overline{n} = \sum n_i$ is the average number density. Here, the "3/2" and "5/2" factors correspond to monotomic and diatomic molecules, respectively. As before, $\gamma = C_p/C_v$. We find $\mathrm{X_{MW}}$ = 16 gm/mole and γ = 1.66.

[52] We calculate N_B via

$$N_B^2 = \frac{g}{\overline{\theta}}\frac{d\overline{\theta}}{dz} = \frac{g}{\overline{T}}\left(\frac{d\overline{T}}{dz} + \frac{g}{C_p}\right). \tag{30}$$

We estimate $d\overline{T}/dz = 0$, since the atmosphere is approximately isothermal at that altitude. This is quite close to the MSIS value of $d\overline{T}/dz = 5 \times 10^{-6}$ K/m. Using $g = 9.8(R_{Earth}/(R_{Earth} + z))^2$ m/s^2, where $R_{Earth} = 6.371 \times 10^6$ m is the radius of Earth, we find N_B = 0.00661 rad/s, which corresponds to τ_B = 15.8 min. From the isothermal expression $\mathcal{H} = \mathrm{R}\overline{T}/g$, we obtain $\mathcal{H} \sim 75$ km. This agrees reasonably well with the MSIS value of $\mathcal{H} = 80$ km. Finally, using $c_s = \sqrt{\gamma g \mathcal{H}}$, we estimate c_s = 950 m/s. Although the atmosphere is quite rarified at $z \sim 560$ km, we assume that $\mu = 3.34 \times 10^{-4}\overline{T}^{0.71}$ gm/m/s. This yields $\nu = \mu/\overline{\rho} = 1.7 \times 10^7$ m^2/s.

[53] Using the values estimated in the previous paragraph lead to solutions which have phase shifts and amplitude ratios within the necessary ranges; however, $\lambda_{\rm track}$ is somewhat too large. Slightly decreasing $\mathcal{H}$ to 65 km and ν to 1.5×10^7 m^2/s, however, yields solutions which have phase shifts, amplitude ratios and $\lambda_{\rm track}$ within the observed ranges.

[54] Figure 16 shows the theoretical phase shifts, amplitude ratios, and intrinsic periods as a function of λ_H and λ_z for $\mathcal{H}$ = 65 km, c_s = 1000 m/s, $\nu = 1.5 \times 10^7$ m^2/s, γ = 1.66, and N_B = 0.00661 rad/s. Because the phase shift between ρ' and w' is only less than 60° for $|\lambda_z|$ > 1000 km, we only show the results for $|\lambda_z|$ > 1000 km. However, since $4\pi\mathcal{H} \sim$ 820 km, we note that we might be stretching the validity of this theory if a GW with $|\lambda_z|$ > 820 km is strongly dissipating. A better understanding of the validity of the theory for strongly dissipating GWs with $|\lambda_z| > 4\pi\mathcal{H}$ will be determined numerically in a future work.

[55] Figures 16b and 16c show that w' always leads ρ' and T' always leads w' in distance along the direction of GW propagation. This means that if the satellite is traveling in the same direction as the wave, it first encounters a peak in ρ', then w', then T'. (This can be seen in Figures 2a, 2c, or 2e, by moving a satellite along the +x direction (i.e., along the GW propagation direction).) Combining this with the observations, we see that the GW was propagating in the same direction as the satellite, in agreement with IC02. Since the satellite was propagating southward after 22.08 UT, we conclude that the meridional component of the GW's propagation direction was southward at that time. We show the small region of overlap for 5 constraints (the $w' - T'$, $w' - \rho'$, and $T' - \rho'$ phase shifts, $(\rho'_0/\overline{\rho})/w'_0$, and $\left(T'_0/\overline{T}\right)/(\rho'_0/\overline{\rho})$), as the pink hatched region in Figure 16e. The fact that these constraints, 4 of which are independent, overlap at all is remarkable. Figure 16e also shows ϵ. For all of the GWs within the overlap region, $0.5 \leq \epsilon \leq 1$; these GWs are slightly above the altitude where their momentum fluxes are maximum, implying they are not (yet) strongly dissipating. This likely lessens the severity of the assumption that $|\lambda_z| < 4\pi\mathcal{H}$, although we do not know by how much. Only those GWs with $\epsilon \ll 1$ are strongly dissipating.

[56] We now infer the GW propagation direction ψ, using

$$\psi = \cos^{-1}\left(u'_{track,0}/u'_{H0}\right). \tag{31}$$

For this overlap region, the phase shift between w' and u'_H is ≤20° from Figure 16a. Since the phase of u'_{track} equals the phase of u'_H, and since the phase difference between w' and u'_{track} was <50°, we conclude that the GW was propagating in an eastward direction, in agreement with IC02. We use $w'_0 \sim 110$ m/s and the observed cross-track (zonal) wind perturbation amplitude from Figures 1 and 6 of IC02 of $u'_{track,0} \sim 110$ m/s. We then calculate u'_{H0} from Figure 16a. A blow-up of the overlap region and ψ are shown in Figure 16f. We also calculate the distance between wave crests along the satellite path of

$$\lambda_{\rm track} \sim \lambda_H/\sin(\psi), \tag{32}$$

where we have used equation (25) with $\phi = 90 - \psi$. For these background parameters, the GWs in the overlap region have horizontal wavelengths of λ_H = 600 − 630 km, distance between wave crests (as seen by the satellite) of $\lambda_{\rm track}$ = 700 − 750 km, and southeastward propagation directions of ψ = −(55 − 57)°.

[57] We now allow the background parameters to vary: $\mathcal{H} = 60 - 75$ km, ν = (1.0 − 2.0) × 10^7 m^2/s, and c_s = 1000 − 2000 m/s. We set N_B = 0.00661 rad/s and γ = 1.66. Figure 17 shows the GW solutions for which the $w' - T'$, $w' - \rho'$, and $T' - \rho'$ phase shifts, $(\rho'_0/\overline{\rho})/w'_0$, $\left(T'_0/\overline{T}\right)/(\rho'_0/\overline{\rho})$, and $\lambda_{\rm track}$ fall within the observed values (solid lines). These GWs have λ_H = 500 − 625 km, $|\lambda_z|$ = 1000 − 2500 km, ψ = −(40 − 60)°, τ_{Ir} = 16 − 17 min, c_{IH} = 525 − 650 m/s, and ϵ = 0.5 − 1.5. Here, the intrinsic phase speed is $c_{IH} = \omega_{Ir}/k_H$. Since c_{IH} is ~9% of the satellite velocity, our assumption that the satellite took a snapshot of the wave is reasonable. Note that the large value of $|\lambda_z|$ and small intrinsic period inferred from these

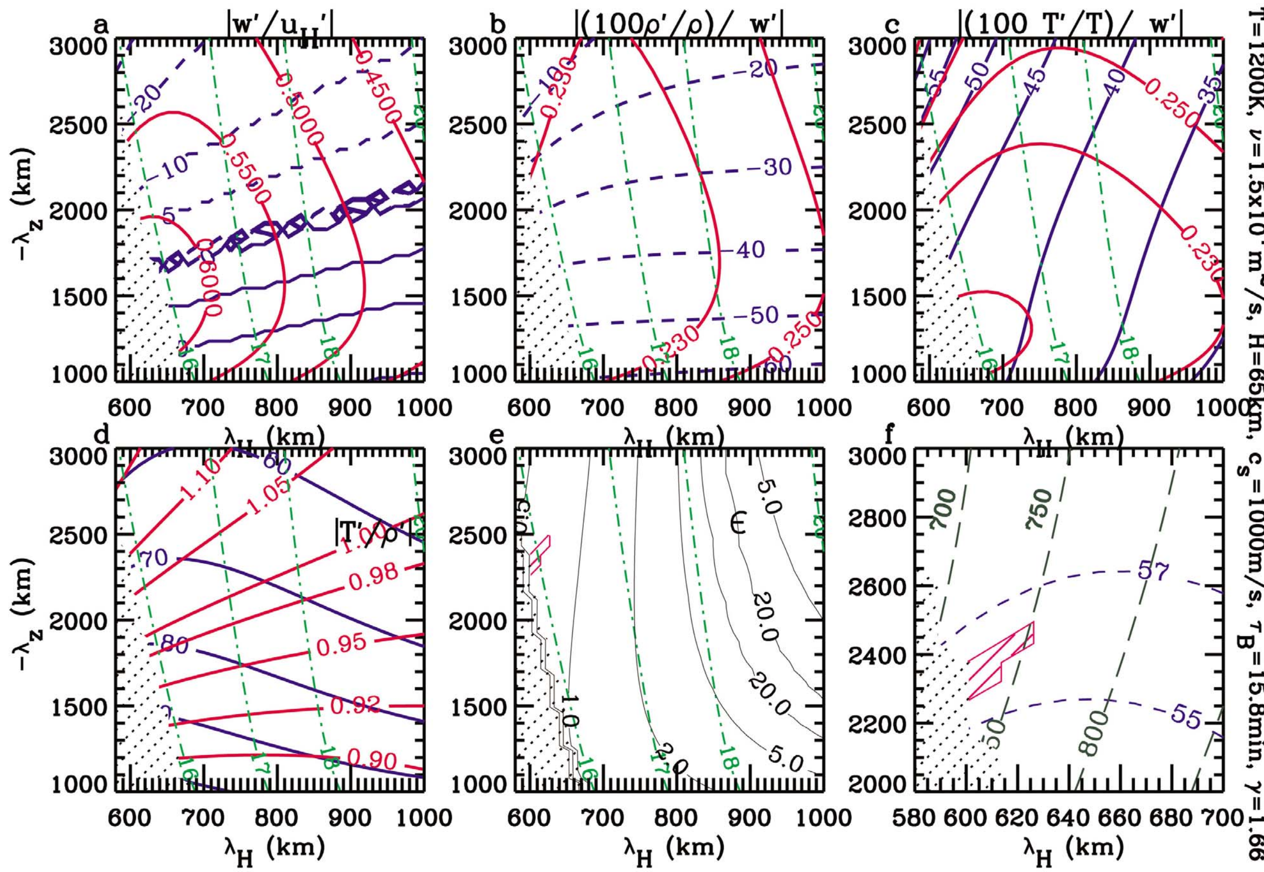

Figure 16. Phase shifts in degrees (blue) and amplitude ratios (red) for a thermosphere with $\overline{T} = 1200$ K, $\nu = 1.5 \times 10^7$ m^2/s, $\mathcal{H} = 65$ km, $\gamma = 1.66$, $c_s = 1000$ m/s, and $\tau_B = 15.8$ min. (a) w' with respect to u'_H. (b) $\rho'/\overline{\rho}$ with respect to w'. (c) $T'/\overline{T}$ with respect to w'. (d) $T'/\overline{T}$ with respect to $\rho'/\overline{\rho}$. Solid (dash) blue lines denote positive (negative) values. (e) Region of overlap between the constraints (pink hatched lines), as described in the text. The dissipation factor ϵ (from equation (24)) is shown as black lines. Green dash-dot lines show the intrinsic GW period τ_{Ir} (in minutes) in Figures 16a–16e. (f) Blow-up of the overlap region (pink hatched lines). $\lambda_{\rm track}$ (in km) is shown as dark green long-dash lines, and ψ (in deg) is shown as blue dash lines.

observations is not surprising, since GWs which reach such high altitudes must have large $|\lambda_z|$ and ω_{Ir} [*Vadas*, 2007; *Fritts and Vadas*, 2008]. We also show the non-dimensional GW amplitude in Figure 17g:

$$u'_H/c_{IH}. \tag{33}$$

This amplitude ranges from $\sim$0.25–0.35; therefore, although this GW has a large amplitude, it is not breaking [*Fritts and Alexander*, 2003]. Note that the estimated intrinsic period is only slightly larger than the buoyancy period of $\tau_B = 15.8$ min. This estimated period is in good agreement with the result of IC02 of 13 or 17 min.

[58] The vertical wavelengths in Figure 17b might seem excessively large; however, λ_z is a measure of the vertical derivative of the slope of the phase line. If a GW propagates against the background wind such that its intrinsic frequency approaches the buoyancy frequency, $|\lambda_z|$ increases dramatically. Indeed, extremely large vertical wavelengths of $|\lambda_z| \sim 2000$–3000 km were inferred from the phase lines of GWs with smaller horizontal wavelengths of $\lambda_H \sim 200$–250 km [*Vadas and Nicolls*, 2009, Figure 8b]. In that case, there was a strong wind at $z \sim 180$–200 km in a direction opposite to the GW propagation direction which caused such large values; above that altitude, $|\lambda_z|$ was much smaller.

[59] In Figure 17, we also show those solutions with $\mathcal{H} \geq 65$ km and $\nu \geq 1.5 \times 10^7$ m^2/s as dotted lines. For these GW solutions, $\lambda_H = 600 - 625$ km, $|\lambda_z| \sim 2200$–2500 km, $\psi = 55 - 60^{\rm o}$, and $\tau_{Ir} = 16$ min. Additionally, $\epsilon \sim 0.6 - 0.7$, which implies that the momentum fluxes of the GWs are beginning to decrease with altitude. These "dotted" solutions might be considered the "best" solutions, because $\mathcal{H}$ and ν are closest to their estimated values.

5. Conclusions

[60] In this paper, we derived the compressible dispersion and polarization relations for high-frequency GWs and AWs dissipating in the thermosphere from kinematic viscosity and thermal diffusivity. The source of the GWs and AWs was assumed to be time-dependent and spatially localized, not steady state and horizontally uniform as assumed by full wave models. Additionally, several compressible, dissipative

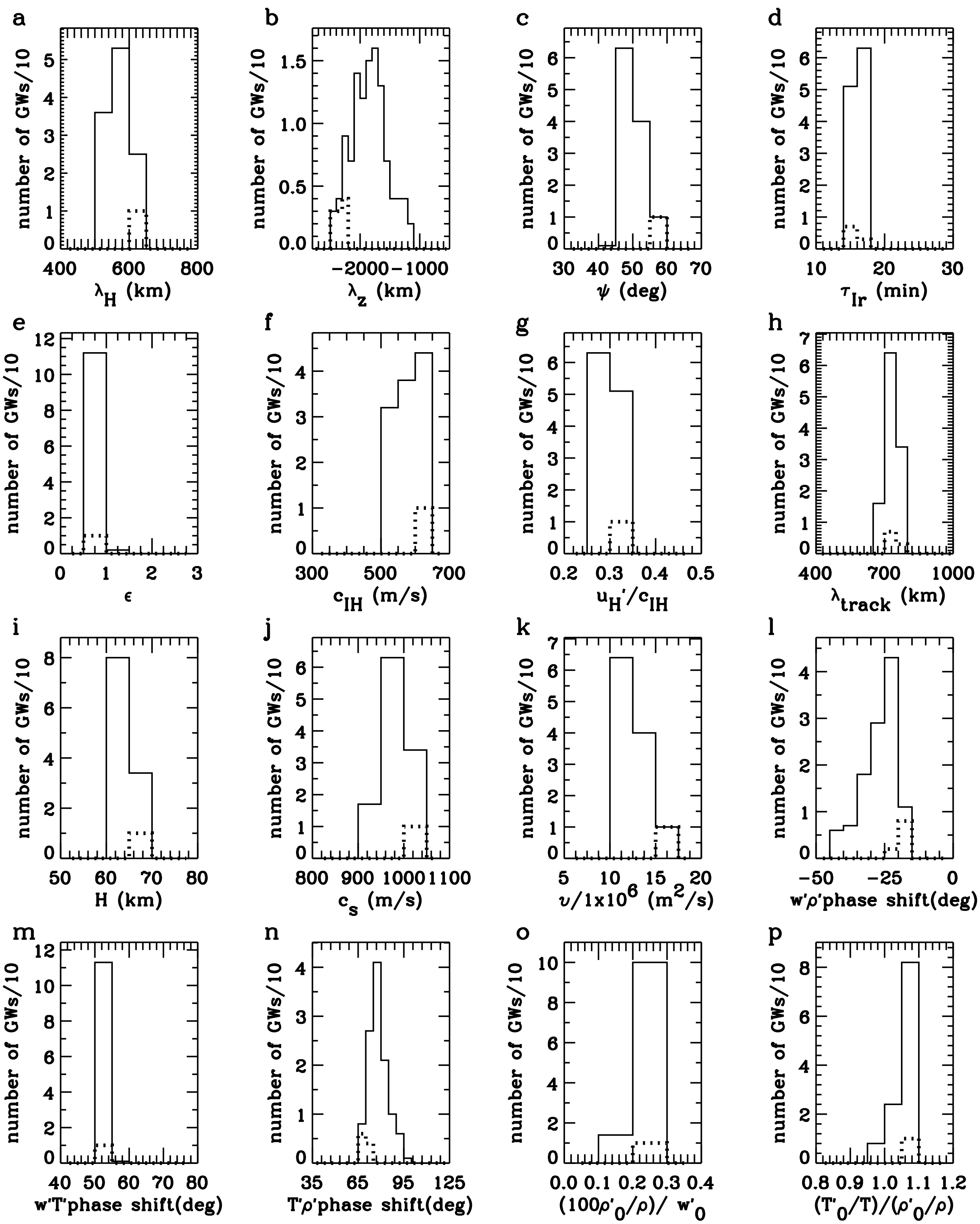

Figure 17. GW solutions for the 5 independent constraints (solid lines), as described in the text. (a) λ_H. (b) λ_z. (c) ψ. (d) τ_{Ir}. (e) ϵ (see equation (24)). (f) c_{IH} (g) u'_H/c_{IH}. (h) λ_{track}. (i) $\mathcal{H}$. (j) c_s. (k) $\nu/1 \times 10^6$. (l) $w' - \rho'$ phase shift. (m) $w' - T'$ phase shift. (n) $T' - \rho'$ phase shift. (o) $(100\rho'_0/\overline{\rho})/w'_0$. (p) $(T'_0/\overline{T})/(\rho'_0/\overline{\rho})$. Dotted lines show the subset of solutions for which $\mathcal{H} = 65$ km and $\nu = 1.5 \times 10^7$ m^2/s. Phase shifts are in degrees.

terms neglected in VF05 were included here, although we find that they are not, in general, very important. We showed that the phase shifts and amplitude ratios of GWs with $|\lambda_z| \gg \mathcal{H}$ cannot be described by the Boussinesq relations, as they are significantly affected by compressibility. For example, as $|\lambda_z|$ increases, the phase shift between u'_H and w' decreases from 0 to $\sim -90°$, and the phase shift between T' and ρ' decreases from 180 to 0°. We also showed that the phase shifts and amplitude ratios depend on the exospheric temperature of the thermosphere (ranging here from $\overline{T} = 600 - 1500$ K), $\mathcal{H}$, the buoyancy frequency N_B, and ν.

[61] As with any analytic theory, the solutions derived in this paper involve assumptions and approximations. The main assumption of this theory is that the sources of the GWs and AWs are spatially and temporally localized. The main approximations of this theory are that the wave is linear, and that $|\lambda_z| < 4\pi\mathcal{H}$ if the GW is strongly dissipating. We emphasize that this last criteria, $|\lambda_z| < 4\pi\mathcal{H}$, is only relevant if the GW is strongly dissipating. If the GW is not strongly dissipating (i.e., has an amplitude which is growing nearly exponentially with altitude), then this criteria does not apply because the assumption that ν be locally constant is irrelevant. If the GW is dissipating and $|\lambda_z| > 4\pi\mathcal{H}$, however, it is not known how "incorrect" the predictions of this theory are. This question could likely be answered by targeted 2D numerical fluid simulations of dissipating wave packets from temporally and spatially variable GW sources.

[62] We showed in this paper that the dissipative, compressible polarization and dispersion relations can be used to "fill-in-the-gap" when data is missing or cannot be measured, such as λ_H, λ_z, ω_{Ir}, and ψ for GWs observed in-situ by satellites. Using examples, we showed how these relations can be used to estimate a GW's λ_H, λ_z, ω_{Ir}, and direction of propagation ψ for in-situ satellite observations of (1) the 3D neutral wind perturbations or (2) ρ', T', w', and u'_{track}. These deduced GW parameters are important for reverse ray tracing in order to identify their sources.

[63] As a test of this theory, we analyzed one of the GWs observed by the instruments aboard the DE2 satellite. This GW was discussed by IC02. We found a relatively confined region in GW parameter space such that the observed phase shifts, amplitude ratios, and $\lambda_{\rm track}$ overlapped. This was remarkable, considering the independent nature of these 5 quantities (in principle). Using these constraints, we estimated the GW to have $\lambda_H = 600 - 625$ km, $\lambda_z \sim -(2200–2500)$ km, $\psi = -(55 - 60)°$, and $\tau_{Ir} \sim 16–17$ min. Since these constraints were independent, we view this overlap as a reasonable test and validation of this theory. From the result of this study and that presented in the companion paper, we conclude that the GW polarization and dispersion relations derived herein can be utilized (with caution) to estimate a GW's λ_H, λ_z, ω_{Ir}, and ψ from in-situ satellite measurements of GWs with $\epsilon > 0.5$.

Notation

- c_s, N_B Speed of sound, buoyancy frequency.
- $\mathcal{H}$, ν Density scale height, kinematic viscosity.
- $\overline{T}$, $X_{\rm MW}$ Background temperature, mean molecular weight.
- $\overline{\rho}$,C_p,C_V Mean density, heat capacity at constant pressure and volume.
- λ_H Horizontal wavelength (>0).
- λ_x, λ_y Zonal (+ if east) and meridional (+ if north) components of λ_H.
- λ_z Vertical wavelength (<0 if upward-propagating).
- c_H Observed horizontal phase speed.
- c_{IH} Intrinsic horizontal phase speed.
- τ_{Ir} Intrinsic wave period.
- ϵ Dissipation factor (defined in equation (24)).
- u'_H Horizontal component of wave perturbation velocity.
- w' Vertical component of wave perturbation velocity.
- T' wave temperature perturbation.
- ρ' wave density perturbation.
- w'_0,ρ'_0. Amplitudes of vertical velocity and density perturbations (>0).
- $\lambda_{\rm track}$ Apparent wavelength along satellite track (>0).
- ψ Propagation direction counter-clockwise (north) of east.

[64] **Acknowledgments.** SLV would like to thank John Meriwether for helpful comments, and Mark Conde for DE2 information. SLV was supported by NSF grant ATM-0836195, and NASA contracts NNH08CE12C and NNH10CC98C. MJN was supported by NSF grant AGS-0836142. The Dynamics Explorer-2 (DE 2) Neutral Atmosphere Composition Spectrometer (NACS) and Wind and Temperature Spectrometer (WATS) Data was obtained through the NASA National Space Science Data Center.

[65] Robert Lysak thanks the reviewers for their assistance in evaluating this paper.

References

Bauer, S. J. (1958), An apparent ionospheric response to the passage of hurricanes, *J. Geophys. Res.*, *63*, 265–269.

Bishop, R., N. Aponte, G. D. Earle, M. Sulzer, M. Larsen, and G. Peng (2006), Arecibo observations of ionospheric perturbations associated with the passage of tropical storm Odette, *J. Geophys. Res.*, *111*, A11320, doi:10.1029/2006JA011668.

Bruinsma, S. L., and J. M. Forbes (2009), Properties of traveling atmospheric disturbances (TADs) inferred from CHAMP accelerometer observations, *Adv. Space Res.*, *43*, 369–376.

Chimonas, G., and C. O. Hines (1970), Atmospheric gravity waves launched by auroral currents, *Planet. Space Sci.*, *18*, 565–582.

Chimonas, G., and W. R. Peltier (1970), The bow wave generated by an auroral arc in supersonic motion, *Planet. Space Sci.*, *18*, 599–612.

Dalgarno, A., and F. J. Smith (1962), The thermal conductivity and viscosity of atomic oxygen, *Planet. Space Sci.*, *9*, 1–2.

DelGenio, A. D., and G. Schubert (1979), Gravity wave propagation in a diffusively separated atmosphere with height-dependent collision frequencies, *J. Geophys. Res.*, *84*, 4371–4378.

Djuth, F. T., M. P. Sulzer, J. H. Elder, and V. B. Wickwar (1997), High-resolution studies of atmosphere–ionosphere coupling at Arecibo Observatory, Puerto Rico, *Radio Sci.*, *32*, 2321–2344.

Djuth, F. T., M. P. Sulzer, S. A. Gonzales, J. D. Mathews, J. H. Elder, and R. L. Walterscheid (2004), A continuum of gravity waves in the Arecibo thermosphere?, *Geophys. Res. Lett.*, *31*, L16801, doi:10.1029/2003GL019376.

Djuth, F. T., L. D. Zhang, D. J. Livneh, I. Seker, S. M. Smith, M. P. Sulzer, J. D. Mathews, and R. L. Walterscheid (2010), Arecibo's thermospheric gravity waves and the case for an ocean source, *J. Geophys. Res.*, *115*, A08305, doi:10.1029/2009JA014799.

Earle, G. D., J. H. Klenzing, W. A. Macaulay, M. D. Perdue, and E. L. Patrick (2007), A new satellite-borne neutral wind instrument for thermospheric diagnostics, *Rev. Sci. Instrum.*, *78*(11), 114501.

Earle, G. D., A. Mwene-Musumba, and S. L. Vadas (2008), Satellite-based measurements of gravity wave-induced mid-latitude plasma density perturbations, *J. Geophys. Res.*, *113*, A03303, doi:10.1029/2007JA012766.

Eckermann, S., and C. Marks (1996), An idealized ray model of gravity wave-tidal interactions, *J. Geophys. Res.*, *101*, 21,195–21,212, doi:10.1029/96JD01660.

Einaudi, F., and C. O. Hines (1970), WKB approximation in application to acoustic-gravity waves, *Can. J. Phys.*, *48*, 1458–1471.

Francis, S. H. (1973), Acoustic-gravity modes and large-scale traveling ionospheric disturbances of a realistic dissipative atmosphere, *J. Geophys. Res.*, *78*, 2278–2301.

Francis, S. H. (1975), Global propagation of atmospheric gravity waves: A review, *J. Atmos. Terr. Phys.*, *37*, 1011–1030.

Fritts, D. C., and M. J. Alexander (2003), Gravity wave dynamics and effects in the middle atmosphere, *Rev. Geophys.*, *41*(1), 1003, doi:10.1029/2001RG000106.

Fritts, D. C., and S. Vadas (2008), Gravity wave penetration into the thermosphere: Sensitivity to solar cycle variations and mean winds, *Ann. Geophys.*, *26*, 3841–3861.

Georges, T. M. (1968), HF Doppler studies of traveling ionospheric disturbances, *J. Atmos. Terr. Phys.*, *30*, 735–746.

Gross, S. H., C. A. Reber, and F. T. Huang (1984), Large-scale waves in the thermosphere observed by the AE-C satellite, *IEEE Trans. Geosci. Remote Sens.*, *22*, 340–352.

Hajkowicz, L. A. (1990), A global study of large scale travelling ionospheric disturbances (TIDs) following a step-like onset of auroral substorms in both hemispheres, *Planet. Space Sci.*, *38*, 913–923.

Hanson, W. B., U. Ponzi, C. Arduini, and M. Di Ruscio (1992), A satellite anemometer, *J. Astro. Sci.*, *40*, 429–438.

Hedin, A. E. (1991), Extension of the MSIS thermosphere model into the middle and lower atmosphere, *J. Geophys. Res.*, *96*, 1159–1172.

Hickey, M. P., and K. D. Cole (1987), A quartic dispersion equation for internal gravity waves in the thermosphere, *J. Atmos. Terr. Phys.*, *49*, 889–899.

Hickey, M. P., R. L. Walterscheid, and P. G. Richards (2000), Secular variations of atomic oxygen in the mesopause region induced by transient gravity wave packets, *Geophys. Res. Lett.*, *27*, 3599–3602.

Hickey, M. P., G. Schubert, and R. L. Walterscheid (2009), The propagation of tsunami-driven gravity waves into the thermosphere and ionosphere, *J. Geophys. Res.*, *114*, A08304, doi:10.1029/2009JA014105.

Hines, C. O. (1960), Internal atmospheric gravity waves at ionospheric heights, *Can. J. Phys.*, *38*, 1441–1481.

Hines, C. O. (1964), Minimum vertical scale sizes in the wind structure above 100 km, *J. Geophys. Res.*, *69*, 2847–2848.

Hocke, K., and K. Schlegel (1996), A review of atmospheric gravity waves and traveling ionospheric disturbances, *Ann. Geophys.*, *14*, 917–940.

Hocke, K., and T. Tsuda (2001), Gravity waves and ionospheric irregularities over tropical convection zones observed by GPS/MET radio occultation, *Geophys. Res. Lett.*, *28*, 2815–2818.

Hocke, K., K. Schlegel, and G. Kirchengast (1996), Phases and amplitudes of TIDs in the high-latitude F-region observed by EISCAT, *J. Atmos. Terr. Phys.*, *58*, 245–255.

Hung, R. J., and J. P. Kuo (1978), Ionospheric observation of gravity-waves associated with hurricane Eloise, *J. Geophys. Res.*, *45*, 67–80.

Hunsucker, R. (1982), Atmospheric gravity waves generated in the high-latitude ionosphere: A review, *Rev. Geophys.*, *20*, 293–315, doi:10.1029/RG020i002p00293.

Innis, J. L., and M. Conde (2002), Characterization of acoustic-gravity waves in the upper thermosphere using Dynamics Explorer 2 Wind and Temperature Spectrometer (WATS) and Neutral Atmosphere Composition Spectrometer (NACS) data, *J. Geophys. Res.*, *107*(A12), 1418, doi:10.1029/2002JA009370.

Kelley, M. C. (1997), In situ ionospheric observations of severe weather-related gravity waves and associated small-scale plasma structure, *J. Geophys. Res.*, *102*, 329–335.

Klostermeyer, J. (1972), Numerical calculation of gravity wave propagation in a realistic thermosphere, *J. Atmos. Terr. Phys.*, *34*, 765–774.

Kundu, P. (1990), *Fluid Dynamics*, 638 pp., Academic, San Diego, Calif.

Lighthill, J. (1978), *Waves in Fluids*, 504 pp., Cambridge Univ. Press, Cambridge, U. K.

Liu, H., H. Luhr, S. Watanabe, W. Kohler, V. Henize, and P. Visser (2006), Zonal winds in the equatorial upper thermosphere: Decomposing the solar flux, geomagnetic activity, and seasonal dependencies, *J. Geophys. Res.*, *111*, A07307, doi:10.1029/2005JA011415.

Maeda, S. (1985), Numerical solutions of the coupled equations for acoustic-gravity waves in the upper thermosphere, *J. Atmos. Terr. Phys.*, *47*, 965–972.

Mayr, H. G., I. Harris, F. A. Herrero, N. W. Spencer, F. Varosi, and W. D. Pesnell (1990), Thermospheric gravity waves: Observations and interpretation using the transfer function model (TEM), *Space Sci. Rev.*, *54*, 297–375.

Midgley, J. E., and H. B. Liemohn (1966), Gravity waves in a realistic atmosphere, *J. Geophys. Res.*, *71*, 3729–3748.

Nicolls, M. J., S. L. Vadas, J. W. Meriwether, M. G. Conde, and D. Hampton (2012), The phases and amplitudes of gravity waves propagating and dissipating in the thermosphere: Application to measurements over Alaska, *J. Geophys. Res.*, doi:10.1029/2012JA017542, in press.

Oliver, W. L., Y. Otsuka, M. Sato, T. Takami, and S. Fukao (1997), A climatology of F region gravity wave propagation over the middle and upper atmosphere radar, *J. Geophys. Res.*, *102*, 14,499–14,512.

Pitteway, M. L. V., and C. O. Hines (1963), The viscous damping of atmospheric gravity waves, *Can. J. Phys.*, *41*, 1935–1948.

Richmond, A. D. (1978), Gravity wave generation, propagation, and dissipation in the thermosphere, *J. Geophys. Res.*, *83*, 4131–4145.

Röttger, J. (1977), Travelling disturbances in the equatorial ionosphere and their association with penetrative cumulus convection, *J. Atmos. Terr. Phys.*, *39*, 987–998.

Salby, M. L., and R. R. Garcia (1987), Transient response to localized episodic heating in the tropics. Part I: Excitation and short-time, near-field behavior, *J. Atmos. Sci.*, *44*(2), 458–498.

Tsugawa T., A. Saito, Y. Otsuka, and M. Yamamoto (2003), Damping of large-scale traveling ionospheric disturbances detected with GPS networks during the geomagnetic storm, *J. Geophys. Res.*, *108*(A3), 1127, doi:10.1029/2002JA009433.

Vadas, S. L. (2007), Horizontal and vertical propagation and dissipation of gravity waves in the thermosphere from lower atmospheric and thermospheric sources, *J. Geophys. Res.*, *112*, A06305, doi:10.1029/2006JA011845.

Vadas, S. L., and G. Crowley (2010), Sources of the traveling ionospheric disturbances observed by the ionospheric TIDDBIT sounder near Wallops Island on October 30, 2007, *J. Geophys. Res.*, *115*, A07324, doi:10.1029/2009JA015053.

Vadas, S. L., and D. C. Fritts (2001), Gravity wave radiation and mean responses to local body forces in the atmosphere, *J. Atmos. Sci.*, *58*, 2249–2279.

Vadas, S. L., and D. C. Fritts (2005), Thermospheric responses to gravity waves: Influences of increasing viscosity and thermal diffusivity, *J. Geophys. Res.*, *110*, D15103, doi:10.1029/2004JD005574.

Vadas, S. L., and D. C. Fritts (2006), Influence of solar variability on gravity wave structure and dissipation in the thermosphere from tropospheric convection, *J. Geophys. Res.*, *111*, A10S12, doi:10.1029/2005JA011510.

Vadas, S. L., and D. C. Fritts (2009), Reconstruction of the gravity wave field from convective plumes via ray tracing, *Ann. Geophys.*, *27*, 147–177.

Vadas, S. L., and H.-L. Liu (2009), The generation of large-scale gravity waves and neutral winds in the thermosphere from the dissipation of convectively-generated gravity waves, *J. Geophys. Res.*, *114*, A10310, doi:10.1029/2009JA014108.

Vadas, S. L., and H.-L. Liu (2011), Neutral winds and densities at the bottomside of the F layer from primary and secondary gravity waves from deep convection, in *Aeronomy of the Earth's Atmosphere and Ionosphere*, pp. 131–139, Springer, New York.

Vadas, S. L., and M. J. Nicolls (2008), Using PFISR measurements and gravity wave dissipative theory to determine the neutral, background thermospheric winds, *Geophys. Res. Lett.*, *35*, L02105, doi:10.1029/2007GL031522.

Vadas, S. L., and M. J. Nicolls (2009), Temporal evolution of neutral, thermospheric winds and plasma response using PFISR measurements of gravity waves, *J. Atmos. Sol. Terr. Phys.*, *71*, 740–770.

Volland, H. (1969a), The upper atmosphere as a multiply refractive medium for neutral air motions, *J. Atmos. Terr. Phys.*, *31*, 491–514.

Volland, H. (1969b), Full wave calculations of gravity wave propagation through the thermosphere, *J. Geophys. Res.*, *74*,1786–1795.

Waldock, J. A., and T. B. Jones (1987), Source regions of medium scale travelling ionospheric disturbances observed at mid-latitudes, *J. Atmos. Terr. Phys.*, *49*, 105–114.

Walterscheid, R. L., and M. P. Hickey (2011), Group velocity and energy flux in the thermosphere: Limits on the validity of group velocity in a viscous atmosphere, *J. Geophys. Res.*, *116*, D12101, doi:10.1029/2010JD014987.

Yanowitch, M. (1967), Effect of viscosity on gravity waves and the upper boundary condition, *J. Fluid Mech.*, *29*, 209–231.

Yeh, K. C., and C. H. Liu (1974), Acoustic-gravity waves in the upper atmosphere, *Rev. Geophys.*, *12*, 193–216, doi:10.1029/RG012i002p00193.

Yeh, K. C., C. H. Liu, and M. Y. Youakim (1975), Attenuation of internal gravity waves in model atmospheres, *Ann. Geophys.*, *31*, 321–328.